A Study of the Aeroelastic Behavior of Flat Plates and Membranes with Mixed Boundary Conditions in Axial, Subsonic Flow: Theory

by

Elizabeth M. Bloomhardt

Department of Mechanical Engineering and Materials Science
Pratt School of Engineering
Duke University

Date:________________________
Approved:

____
Earl H. Dowell, Supervisor

____
Donald B. Bliss

____
Kenneth C. Hall

Thesis submitted in partial fulfillment of
the requirements for the degree of Master of Science in the Department of
Mechanical Engineering and Materials Science in the Graduate School
of Duke University

2011

ABSTRACT

A Study of the Aeroelastic Behavior of Flat Plates and Membranes with Mixed

Boundary Conditions in Axial, Subsonic Flow: Theory

by

Elizabeth M. Bloomhardt

Department of Mechanical Engineering and Materials Science
Duke University

Date:_______________________
Approved:

____
Earl H. Dowell, Supervisor

____
Donald B. Bliss

____
Kenneth C. Hall

An abstract of a thesis submitted in partial
fulfillment of the requirements for the degree
of Master of Science in the Department of
Mechanical Engineering and Materials Science in the Graduate School
of Duke University

2011

Abstract

In support of the noise reduction targets for future generations of transport aircraft, as set forth by NASA, the fundamental aeroelastic behavior of trailing edge flap technology was explored. Using a plate structural model to approximate the structural configuration and linear potential flow theory to represent the aerodynamics, aeroelastic behavior was characterized for two structural configurations using two different sets of boundary conditions for each. The two structural configurations considered were a) all edges fixed and b) leading and side edges fixed, trailing edge free. In each configuration both simply supported and clamped boundary conditions were considered. Results are compared to calculations presented in the literature for the all edges simply supported configuration.

Dedication

To: my Mom

Contents

List of Tables

List of Figures

Nomenclature

Structural Terms

ω	=	natural frequency
ν	=	Poisson's ratio
ζ	=	damping ratio
ρ_m	=	material density
Ψ	=	assumed structural mode shape
D	=	stiffness
E	=	Young's modulus
I	=	second moment of inertia
L	=	Lagrangian
M_{mnkl}	=	mass matrix
K_{mnkl}	=	stiffness matrix
T_x	=	tension in the x-direction
T_y	=	tension in the y-direction
δW	=	virtual work
m_s	=	mass of structure
a	=	nominal length, flow direction
b	=	nominal length, cross-flow direction
h	=	material thickness

h_f = material thickness factor

q = generalized coordinate

w = out of plane displacement

x = chordwise coordinate direction parallel to mean flow

y = spanwise coordinate direction perpendicular to mean flow

z = coordinate direction out-of-plane

Aerodynamic Terms

α = Fourier transform variable

γ = Fourier transform variable

ϕ = velocity potential

ρ = air mass density

M = Mach number

Q = non-dimensional aerodynamic force

S_{mnkl} = Piston Theory coefficient

D_{mnkl} = Piston Theory coefficient

H_{mnkl} = Influence function

I_{mnkl} = Influence function

G_{mnkl} = Influence function integrand

U_{∞} = flow speed

Δp = pressure differential across structure

a_∞ = speed of sound

Aeroelastic Terms

λ = non-dimensional dynamic pressure, $\rho U_\infty^2 \frac{a^3}{D}$

μ = mass ratio, $\frac{\rho a}{\rho_m h}$

t = time

s = non-dimensional time, $s = tU/a_\infty$

General Notation

~ = non-dimensional form

$\dot{}$ = first time derivative

$\ddot{}$ = second time derivative

m, n, k, l = counting indices

Acknowledgements

Graduate school thus far has been a wonderful journey and there are numerous people that have enabled me to reach this milestone.

I first owe a great thanks to my advisor at Duke, Earl Dowell for allowing me the freedom of responsibility and enduring with me the false starts, diversions and trying moments that invariably lead to discoveries and learning. I have learned much that I respect and admire of his approach and passion for his work. Also at Duke have been other faculty who have captured my attention and the two others to whom I am most indebted are my committee members, Kenneth Hall and Donald Bliss. May they forever fight over who taught me more (and hopefully do so at E-socials)!

Now a word to my sponsors! This work has been generously supported in part by the Graduate Student Research Program (GSRP) at the National Aeronautics and Space Administration (NASA) Langley Research Center (LaRC) in Hampton, VA. I owe a special thanks to my NASA advisor, Jennifer Heeg, and to Sandra Myers, the GSRP program administrator, as well as my fellow GSRP Fellows. You’ve each made me feel welcome on each of my visits and inspired awe of all that goes on in the impressive facilities at NASA LaRC.

In addition, my colleagues in the trenches at Duke are equally to blame for my accomplishments. My officemates, first the honorable Dr. Justin Jaworski, and later Ivan Wang, both deserve special recognition for their time, tolerance and advice. The rest of my research group, past and present: the basement guys, Dr's Howard Conyers and Chad Custer, and later Chad Gibbs as well as Maciej Balajewicz and all the undergrads who filtered through – your intelligence and perspective have been invaluable. In addition, thanks to Ted Lyman and Stephen Clark for helping to fill up classes with their smarts and homework help among other things. And of course, to those in the MEMS office, Kathy Parrish especially – thanks for all you do!

I have not stayed in my office during my tenure to date at Duke and for those that have encouraged and enabled me I am eternally grateful. I have met many wonderful, engaging and diverse people in my wanderings both within and beyond Pratt that I am forever changed. One of my favorite escapes happens on the trails, which has made the discovery of my kindred spirits, The TrailHeads, Inc. all the more sweet.

Finally, I owe everything to my family. First to my parents, for EVERYTHING! And last, but hardly least, Kyle: for coming with, being there, and making me laugh now and forrrreeeevvvvrrrrr!

1. Introduction

1.1. Motivation and Literature Review

The motivation for the work undertaken herein is the advancement of the state of the art in aeronautical noise reduction technology and a deeper understanding of the fundamental aeroelastic behavior of flat plates and membranes with mixed boundary conditions.

1.1.1. NASA: Noise

The National Aeronautic Space Administration (NASA) Strategic Plan of 2000 set forth four goals under the Aerospace Technology enterprise, the first of which is to revolutionize aviation. To do so, the Strategic Plan identifies five areas fundamental to the expansion of global civilian aviation, specifically improvements in passenger safety, throughput and mobility, as well as improvements in noise and emissions. (1)

Forecasts by various federal agencies including the Federal Aviation Administration (FAA) continue to predict an increase in aviation traffic over the next 25-35 years (2). Congressional action to address the perceived imminence of the problems this growth will precipitate led to the creation of the Joint Planning and Development Office (JPOD) in 2003 to generate the vision for the Next Generation Air Transportation System (NGATS) and define the advancements needed to achieve that vision. NASA's research objectives for noise suppression are in support of the goals set forth by JPDO and the requirements for the NextGen objectives. (3) (4)

In late 2005 and 2006, the Fundamental Aeronautics Subsonic Fixed-Wing Project took shape within NASA to address the goals set forth in the Strategic Plan of 2000 for the next several generations of transport aircraft. The new research project's stated mission is to develop "prediction methods and technologies that will produce lower noise, lower emissions, and higher performing subsonic aircraft for the Next Generation Air Transportation System" (5). Over the course of the project's development, targets in each category, noise, emissions and performance, were set for the next three generations, N+1-3, of transport aircraft slated to come into service in 2015, 2020-2025, and 2030-2035 respectively (6).

While the strategic plan was being formulated, researchers at NASA were quantifying, sourcing and modeling the physics behind the noise problem. Airframe noise accounts for more than half of the perceived noise, or acoustic signature of the aircraft in landing. While the landing gear is the largest contributor to airframe noise, the noise contributions from the wing's control surfaces are also significant. (7)

A 2002 report (8) by NASA's Noise Reduction Program chronicled some of the results of a five year effort, conducted in partnership with industry and academia, to study airframe noise (AFN), in particular, focusing on the high-lift structures known to contribute significantly to airframe noise when the aircraft is in its high-lift configuration on approach. The NASA Langley team employed microphone arrays during wind-tunnel experiments to quantify sound levels, then employed both experimental and computational flow field visualization techniques to identify flow field features that could be responsible for the generation of large noise signatures. Of particular motivating interest to the study described herein, the findings indicate that the noise generation associated with the flaps, located at the trailing edge of the wing, is due to instabilities in both the shear layer, the shedding vortex at the side-edge of the flap, and the interaction between the two, but likely dominated by the vortex as it is convected past the trailing edge of the flap. (8) (9)

Several attempts to disrupt the noise generating flow formations with structural modifications to the flap were also explored and tested in the wind-tunnel with various levels of success. In one case, the side edges of the flap were rounded, in another tabbed indentations were cut into the top or bottom of the flap side-edge to “thicken the mixing region and decrease mean shear” making the shear layer more stable. Another proposal to add serrations, also called a noise weeder, to the trailing edge of the flap was explored experimentally in conjunction with microtabs with moderate success. (8)

Additionally, and of particular interest to the intent of this study is the significant reduction in the magnitude of the acoustic signature that has been demonstrated experimentally when a solid plate structure has been placed to span the gap from the side edge of the deployed control flap to the wing (10). This structure, termed a “continuous mold link” (CML) in the literature, eliminates the discontinuity at the flap side-edge. The smooth transition from the side-edge of the control surface to the trailing edge of the abutting wing section, delays the formation of the vortex generated at that transition. The resulting disruption of the noise generating flow formation results in a significantly lower acoustic signature in the high-lift configuration.

A 2009 evaluation of progress toward the first generation, N+1, noise reduction goal of -32 EPNdB by Berton et. al. suggests that while significant progress has been made, a "3EPNdB shortfall indicates that a slightly greater reliance on noise reduction technologies will be needed to achieve the goal" (11). The study uses a "notional airplane in the 'low-noise corner' of the design trade space," combining an inherently quiet engine design with "innovative, advanced, noise reduction technologies," including CMLs (11). The importance of maturing noise reduction technologies to reach N+1 and future generations of noise reduction targets is clearly demonstrated.

Implementation of the prototype CML technology for the purposes of noise reduction will require maturity to a more compact configuration so as not to sacrifice lifting surface area on the control surface. The design space may also require the use of novel materials, for instance a flexible elastomer that can be stored in a minimal gap between the airframe structures and withstand large stress concentrations and loading when deployed.

Before the analysis of complex flow field simulations and structural finite element modeling are undertaken, it is important to understand the fundamental behavior of this conceptual CML technology, that is, on a fundamental level the aeroelastic behavior of a flexible plate, with mixed boundary conditions.

1.1.2. Aeroelasticity of Plates

The aeroelastic examination of flat plates has been extensively examined under several orientation and boundary condition configurations and in several flow regimes. It is a fundamental structure, whose behavior is helpful in predicting that of more complex geometries and flow field conditions.

Findings from previous studies (12) (13) suggest that the key parameters in determining both the type and amplitude of the aeroelastic behavior of the structure will be the boundary conditions and the orientation in the flow field. For instance, the aeroelastic behavior of plates with regular, simply supported boundary conditions on all sides is well understood (12). A static instability with a deflection on the order of the thickness of the plate dominates and can be characterized as aeroelastic buckling or divergence. Conversely, plates with only the leading edge fixed, exhibit aeroelastic response behavior that can be characterized as plate flutter and which can grow in amplitude to be on the order of a significant fraction of the chord of the structure (13). This configuration has recently been studied at Duke University for its potential in energy harvesting applications (14) (15). Rotating the fixed edge's orientation in the flow field, so that the side edge is fixed, results in the configuration most closely resembling a wing. This configuration is also well understood aeroelastically and is characterized as wing flutter. Wing flutter often involves a coupling of the low bending and torsional modes of the structure. The behaviors classified for the above configurations apply to flow regimes that are subsonic, and are likely to change in supersonic or transonic flow regimes.

Bridging these well understood configurations is the aeroelastic behavior of plates of finite dimension and mixed boundary conditions, i.e. side and leading edges fixed, or just side edges fixed. These configurations and their behavior are less well understood, especially at the low subsonic Mach numbers of interest in the landing approach design space. The research described herein will focus on the configuration in which the leading and side edges are fixed, while the trailing edge remains free.

1.2. Research Questions and Outline

The basic aeroelastic question revolves around the transition to unstable behavior of the system of interest. To this end, an analytical model of increasing complexity can be developed to determine the nature and limits of the system's stability. Chapters 2 and 3 build this analytical model using classic aerodynamic and plate structural theory and employing classic aeroelastic techniques. Chapter 2 also lays out the variations in the plate boundary conditions and corresponding structural theory that comprise the different cases of the study described herein.

Chapter 4 expands upon the additional parameters of interest in determining and classifying the aeroelastic behavior. Included is a discussion of specific study parameters including Mach number, material properties, and aerodynamic parameters as well as the method used to determine the stability boundary.

Chapter 5 presents the results of the aeroelastic study, and Chapter 6 discusses those results, addressing several key questions:

- Which structural model and assumed mode shapes should be used to adequately capture the unique condition of the free trailing edge, while achieving modal convergence?
- How do the results of classifying the aeroelastic behavior and quantifying the flutter boundary compare to the results for other configurations?
- With respect to acoustics, do the dominant frequencies correspond to existing or human hearing range acoustic disturbances?

The novel contributions of the research undertaken herein is a theoretical understanding of the aeroelastic behavior of a plate, fixed on two sides and the leading edge in a subsonic, axial flow field. The material parameters used to model the behavior are obtained from the NASA noise reduction working group. Such a configuration will more closely approximate a plate and can be modeled to first approximation as a plate or membrane. The present study seeks to understand the fundamental aeroelastic behavior of such a configuration in the subsonic flow regimes experienced during landing.

Finally, Chapter 7 proposes future work that would be useful in verifying and expanding upon the results and findings presented herein. But first, a discussion of the theory.

2. Structural Model

A graphical rendering of the structural model of interest is shown in Figure 1 where the cartesian directions and dimensions are labeled relative to the direction of the axial flow.

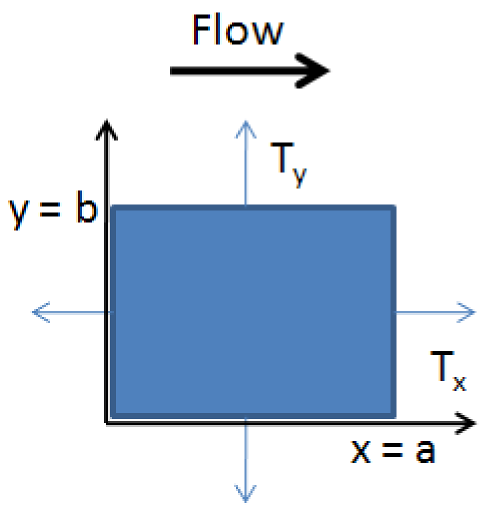

Figure 1 Structural model with cartesian coordinates

Using this classic configuration, the structural equation of motion is as follows (12):

$$\boldsymbol{m_s \frac{\partial^2 w}{\partial t^2} - T_x \frac{\partial^2 w}{\partial x^2} - T_y \frac{\partial^2 w}{\partial y^2} + D\nabla^4 \mathrm{w} + \Delta \mathrm{p} = 0} \qquad (2.1)$$

Here, the acceleration term leads off, followed by two tension terms and a plate/bending stiffness term. The various symbols are defined in the nomenclature. The pressure term, derived from the aerodynamics, is also included as the source of forcing for the system.

2.1. Membrane Model

To a first approximation, the structure can be modeled as a membrane, i.e. $D \equiv 0$. To use energy methods, e.g. Hamilton's Principle or Lagrange's Equations, to determine the equations of motion for the membrane we first start with the kinetic, T, and potential energy, U.

$$\boldsymbol{T = \frac{1}{2}\iint m_s \left(\frac{\partial w}{\partial t}\right)^2 dxdy} \tag{2.2}$$

$$\boldsymbol{U = \frac{1}{2}\iint \left[T_x \left(\frac{\partial w}{\partial x}\right)^2 + T_y \left(\frac{\partial w}{\partial y}\right)^2\right] dxdy} \tag{2.3}$$

In general, the tension, T_x, T_y, and mass, m_s, terms may be allowed to vary with spatial location and are therefore left inside the integrals; w is the membrane deflection; x, y, the spatial coordinates; and t, is time.

Lagrange's Equations. Assume a separable series solution for the out-of-plane deflection,

$$\boldsymbol{w(x,y,t) = \sum_n \Psi_n(x,y) q_n(t),} \tag{2.4}$$

where q_n are the generalized coordinates, and Ψ_n are the mode shapes, or two-dimensional eigen-functions. We can employ Lagrange's equations to derive the equations of motion.

$$\boldsymbol{-\frac{d}{dt}\left(\frac{\partial L}{\partial \dot{q}_i}\right) + \frac{\partial L}{\partial q_i} = 0} \tag{2.5}$$

The Lagrangian, L, is defined as $L \equiv T - U$. Omitting the intermediate steps, we arrive at a generalized equation of motion,

$$\boldsymbol{M_{mn}\ddot{q}_n + K_{mn}q_n = 0}, \tag{2.6}$$

where we have introduced the generalized mass, M_{mn}, and generalized stiffness, K_{mn}, matrices which are defined as follows,

$$\boldsymbol{M_{mn}} \equiv \iint \boldsymbol{m\Psi_m\Psi_n dxdy}, \tag{2.7}$$

$$\boldsymbol{K_{mn}} \equiv \iint \left[\boldsymbol{T_x \frac{\partial\Psi_m}{\partial x}\frac{\partial\Psi_n}{\partial x} + T_y \frac{\partial\Psi_m}{\partial y}\frac{\partial\Psi_n}{\partial y}}\right]\boldsymbol{dxdy}. \tag{2.8}$$

Making the further assumption of harmonic motion,

$$\boldsymbol{q_m = \overline{q}e^{i\omega_n t}}, \tag{2.9}$$

we obtain,

$$\left[\boldsymbol{M_{mn}}\left(-\boldsymbol{\omega_m^2}\right) + \boldsymbol{K_{mn}}\right]\{\boldsymbol{\overline{q}_n}\} = \boldsymbol{0}. \tag{2.10}$$

The quantity, $\bar{q}_n$ is the amplitude of the motion. It cannot be zero for non-trivial solutions. Then, the natural frequencies, ω_n, of the system can be found by setting the determinant of the coefficient system to zero and solving for the frequencies which make this so.

$$\boldsymbol{det}\left[\boldsymbol{M_{mn}}\left(-\boldsymbol{\omega_n^2}\right) + \boldsymbol{K_{mn}}\right] = \boldsymbol{0} \tag{2.11}$$

Hamilton's Principle. An identical result can be arrived at via Hamilton's Principle, stated here:

$$\int_{t_2}^{t_1}[\boldsymbol{\delta T - \delta U}]\boldsymbol{dt} = \boldsymbol{0}. \tag{2.12}$$

Hamilton's Principle introduces the concept of virtual changes in energy and work, represented by the δ symbol seen in Equation (**2.12**). Rather than fully explore this method here, we will simply note that the process of arriving at the generalized equations of motion via Hamilton's Principle also results in the identification of boundary conditions, making it quite useful (12). The form of the generalized equation and the natural boundary conditions that result from its application to the structure discussed herein follows.

$$\mathbf{m_s \frac{\partial^2 w}{\partial t^2} - T_x \frac{\partial^2 w}{\partial x^2} - T_y \frac{\partial^2 w}{\partial y^2} = 0,} \tag{2.13}$$

$$\begin{aligned} \boldsymbol{\left.\frac{\partial w}{\partial x}\right|_{x=0} = 0} \\ \left.\frac{\partial w}{\partial x}\right|_{x=a} = 0 \\ \left.\frac{\partial w}{\partial y}\right|_{y=0} = 0 \\ \left.\frac{\partial w}{\partial y}\right|_{y=b} = 0 \end{aligned} \tag{2.14 a-d}$$

Geometric boundary conditions which arise from formulation of the problem experimentally require that the out-of-plane deflection, w, be zero at one or more edges. In the case of the experimental apparatus used in the Duke wind-tunnel, which informs this theoretical development but is not shown herein, geometric boundary conditions must be imposed at three boundaries as follows:

$$\begin{aligned} \boldsymbol{w|_{x=0} = 0} \\ w|_{x=a} = 0 \\ w|_{y=0} = 0 \end{aligned} \tag{2.15 a-c}$$

The natural boundary condition on the fourth boundary will make up the total of the required boundary conditions for the analytical membrane model.

2.2. Plate Model

Following the development of Dowell (12), we now turn our attention to the analytical plate model. The following development starts with the first principle expressions for energy. Focusing strictly on the elastic potential energy and neglecting the tension effects that were previously included in Equation (**2.1**), the potential and kinetic energy, as well as the virtual work terms can be written as follows:

$$\boldsymbol{U} = \frac{1}{2}\iint \left[\boldsymbol{D_y}\left(\frac{\partial^2 w}{\partial y^2}\right)^2 + \boldsymbol{D_x}\left(\frac{\partial^2 w}{\partial x^2}\right)^2 + 2\boldsymbol{D}\frac{\partial^2 w}{\partial x^2}\frac{\partial^2 w}{\partial y^2} + 4\boldsymbol{D_{xy}}\left(\frac{\partial^2 w}{\partial x \partial y}\right)^2 \right] dxdy \tag{2.16}$$

$$\boldsymbol{T} = \frac{1}{2}\iint m\left(\frac{\partial w}{\partial t}\right)^2 dxdy \tag{2.17}$$

$$\delta W = -\iint (\Delta p \delta w) dxdy \tag{2.18}$$

Applying a Rayleigh-Ritz approximation to the modal expansion, wherein the modes of the structure are assumed such that they satisfy the geometric boundary conditions, the following modal expansion can be made for the out-of-plane displacement, w.

$$w(x, y, t) = \sum_{m=1}^{\infty}\sum_{n=1}^{\infty} q_{mn}(t)\Psi_{mn}(x, y) \tag{2.19}$$

Equation (**2.19**) is then substituted into the energy expressions with the following result:

$$\boldsymbol{U} = \frac{1}{2}\sum_{m}\sum_{k} q_{mn} q_{kl} K_{mnkl} \tag{2.20}$$

$$T = \frac{1}{2}\sum_{m}\sum_{k}\dot{q}_{mn}\dot{q}_{kl}M_{mnkl} \tag{2.21}$$

$$\delta W = -\sum_{k} Q_{kl}\delta q \tag{2.22}$$

where the following have been defined,

$$\begin{aligned} K_{mnkl} = \iint \Bigg[& D_y \frac{\partial^2 \Psi_{mn}}{\partial y^2}\frac{\partial^2 \Psi_{kl}}{\partial y^2} + D_x \frac{\partial^2 \Psi_{mn}}{\partial x^2}\frac{\partial^2 \Psi_{kl}}{\partial x^2} + 2D_1 \frac{\partial^2 \Psi_{mn}}{\partial x^2}\frac{\partial^2 \Psi_{kl}}{\partial y^2} \\ & + 4D_{xy}\frac{\partial^2 \Psi_{mn}}{\partial x \partial y}\frac{\partial^2 \Psi_{kl}}{\partial x \partial y}\Bigg] dxdy \end{aligned} \tag{2.23}$$

$$M_{mnkl} = \iint m\Psi_{mn}\Psi_{kl}dxdy \tag{2.24}$$

$$Q_{kl} = \iint \Delta p\Psi_{kl}dxdy \tag{2.25}$$

To ensure symmetry in the stiffness matrix, an additional computational step is taken by defining a new stiffness matrix as follows. Further discussion will drop the bar.

$$\bar{K}_{mnkl} = \frac{K_{mnkl} + K_{klmn}}{2} \tag{2.26}$$

Once again employing the Legrange equations as described in the previous section, the equations of motion can be written as follows.

$$\sum_{m}\sum_{n} M_{mnkl}\ddot{q}_{mn} + K_{mnkl}q_{mn} + Q_{kl} = 0 \tag{2.27}$$

A similar result can be reached by applying Hamilton's Principle to the energy expressions, Equations (**2.16**) - (**2.18**), which gives the Euler-Legrange equation:

$$D\nabla^4 w + m\frac{\partial^2 w}{\partial t^2} + \Delta p = 0 \tag{2.28}$$

with the associated boundary conditions:

On x = constant

$$w = 0 \text{ or } \frac{\partial^3 w}{\partial x^3} + (2 - \nu)\frac{\partial^3 w}{\partial x \partial y^2} = 0$$

$$\frac{\partial w}{\partial x} = 0 \text{ or } \frac{\partial^2 w}{\partial x^2} + \nu \frac{\partial^2 w}{\partial y^2} = 0$$

On y = constant

$$w = 0 \text{ or } \frac{\partial^3 w}{\partial y^3} + (2 - \nu)\frac{\partial^3 w}{\partial y \partial x^2} = 0$$

$$\frac{\partial w}{\partial y} = 0 \text{ or } \frac{\partial^2 w}{\partial y^2} + \nu \frac{\partial^2 w}{\partial x^2} = 0$$

On x= constant, y = constant (a corner)

$$w = 0 \text{ or } \frac{\partial^2 w}{\partial x \partial y} = 0$$

Galerkin's method for averaging may then be applied after the appropriate modal expansion and orthogonality relationships are identified.

As stated by Dowell, "The essential advantage of the Rayleigh-Ritz approach over Galerkin's method is the choice of [modal] functions" (12). Compared to the Galerkin method, only the geometric boundary conditions must be satisfied by the chosen mode shapes, Ψ_{mn}, in the Rayleigh-Ritz approach. Since the natural mode shapes are not known a priori for the set of boundary conditions of interest, this will prove advantageous.

Further simplifications to the equation of motion, Equation (**2.27**), are possible if the natural modes or orthogonal modes are chosen. Assuming an orthogonal relationship between the modes, the following are true.

$$\int\int \boldsymbol{m\Psi_{mn}\Psi_{kl}\,dxdy = M_{kl}} \qquad \text{for} \quad \boldsymbol{m = k, n = l}$$

$$= 0 \qquad \text{for} \quad m \neq k, n \neq l \tag{2.29}$$

and,

$$\int\int \boldsymbol{D_x \frac{\partial^2\Psi_m}{\partial x^2}\frac{\partial^2\Psi_n}{\partial x^2} + D_y \frac{\partial^2\Psi_m}{\partial y^2}\frac{\partial^2\Psi_n}{\partial y^2} + 2D\frac{\partial\Psi_m}{\partial x}\frac{\partial\Psi_n}{\partial x}\frac{\partial\Psi_m}{\partial y}\frac{\partial\Psi_n}{\partial y} + 4D_{xy}\frac{\partial^2\Psi_m}{\partial x\partial y}\frac{\partial^2\Psi_n}{\partial x\partial y}dxdy = K_{kl}} \qquad \text{for} \quad \boldsymbol{m = k, n = l}$$

$$= 0 \qquad \text{for} \quad m \neq k, n \neq l \tag{2.30}$$

Further, considering the homogenous version of Equation (**2.27**), that is for $\Delta p = 0$, the normal modes and the natural frequencies must satisfy the following formulation.

$$\boldsymbol{M_{mn}(-\omega_{mn}^2) + K_{mn} = 0} \tag{2.31}$$

Which provides an expression for the natural frequencies, ω.

$$\boldsymbol{\omega_{mn}^2 = \frac{K_{mn}}{M_{mn}}} \tag{2.32}$$

These values will, in turn, provide a check on the validity of the assumed theoretical structural mode shapes when compared to natural frequency values obtained experimentally from the physical model.

Up to now, the theoretical development has proceeded in dimensional terms. To enable generalization of trends and comparison to results in the literature a non-dimensionalization scheme consistent with the existing body of work was employed for all analytical calculations. The governing equation, Equation (2.28), takes the following form when the non-dimensional scheme is applied,

$$\begin{gathered}\frac{\partial^4 \tilde{w}}{\partial \tilde{x}^4}+\left(\frac{a}{b}\right)^4 \frac{\partial^4 \tilde{w}}{\partial \tilde{y}^4}+2\nu\left(\frac{a}{b}\right)^2 \frac{\partial^4 \tilde{w}}{\partial \tilde{x}^2 \partial \tilde{y}^2}+2(1-\nu)\left(\frac{a}{b}\right)^2\left(\frac{\partial^2 w}{\partial x \partial y}\right)^2 \\ +\frac{\lambda}{\mu} \frac{\partial^2 \tilde{w}}{\partial s^2}+\Delta \tilde{p}_s=0\end{gathered} \qquad (2.33)$$

where, lambda, λ, and mu, μ, both non-dimensional parameters, are called the dynamic pressure and the mass ratio respectively, and are defined as follows.

$$\lambda \equiv \rho U^2 \frac{a^3}{D}$$

$$\mu \equiv \frac{\rho a}{\rho_m h}$$

The modal relationships for mass, M_{kl}, and stiffness, K_{kl}, can also be expressed in non-dimensional form resulting in a non-dimensional equation of motion as follows.

$$\frac{\lambda}{\mu} \widetilde{M}_n\left[\ddot{q}_n+\widetilde{\omega}_n^2 \tilde{q}_n\right]+\lambda \widetilde{Q}_n=0 \qquad (2.34)$$

To ensure stability in the numerical calculations that will be conducted to explore the behavior of this analytical model, we can further add a structural damping term, where the damping coefficient, ζ, is determined empirically.

$$\frac{\lambda}{\mu} \widetilde{M}_n\left[\ddot{q}_n+2\zeta\widetilde{\omega}_n \dot{q}_n+\widetilde{\omega}_n^2 \tilde{q}_n\right]+\lambda \widetilde{Q}_n=0 \qquad (2.35)$$

To conclude our discussion of the structural model, several aspects of complexity in the assumed mode shapes will now be discussed.

2.3. Modal Expansion

In both the membrane and plate modal expansions that will be discussed herein, the modal approximation for the out-of-plane displacement, w, is expanded as a series expansion that assumes separation of variables in the flow and cross-flow directions, x and y respectively as shown.

$$\boldsymbol{w(x,y,t)} = \sum_{\boldsymbol{m}}\sum_{\boldsymbol{n}} \boldsymbol{q_{mn}(t)\Psi_{mn}(x_m, y_n)} \tag{2.36}$$

For comparison purposes, two boundary condition configurations were considered and each will be described below. In addition, two boundary conditions, clamped and simply supported, were used to help define the mode shapes.

2.3.1. Membrane Modes

Membrane modes consist of one-dimensional sine waves in two directions and satisfy simply supported boundary conditions. A simply supported boundary requires that the out-of-plane displacement at the fixed boundary be zero.

Configuration 1: SSSS

In the first configuration, where all side edges are simply supported, abbreviated "SSSS" in later discussion, the mode shapes are simply sine waves in both the flow and cross-flow directions as shown below.

$$\boldsymbol{\Psi_{mn}(x,y)} = \mathbf{sin}\left(\frac{\boldsymbol{m\pi x}}{\boldsymbol{a}}\right)\mathbf{sin}\left(\frac{\boldsymbol{n\pi y}}{\boldsymbol{b}}\right) \tag{2.37}$$

These modes shapes can also be expressed non-dimensionally.

$$\boldsymbol{\widetilde{\Psi}_{mn}(\tilde{x},\tilde{y})} = \mathbf{sin}(\boldsymbol{m\pi\tilde{x}})\,\mathbf{sin}(\boldsymbol{n\pi\tilde{y}}) \tag{2.38}$$

Configuration 2: SSSF

In the second configuration the leading and side edges are fixed, again simply supported, while the trailing edge is free. The boundary conditions for this case are abbreviated "SSSF" in all later discussion. The mode shapes vary only in the flow direction from the first configuration and are as follows.

$$\boldsymbol{\Psi_{mn}(x,y) = \sin\left(\frac{(2m-1)\pi x}{2a}\right)\sin\left(\frac{n\pi y}{b}\right)} \quad (2.39)$$

which, in non-dimensional form can be written:

$$\boldsymbol{\widetilde{\Psi}_{mn}(\widetilde{x},\widetilde{y}) = \sin\left(\frac{(2m-1)\pi\widetilde{x}}{2}\right)\sin(n\pi\widetilde{y})} \quad (2.40)$$

To simplify the calculations somewhat, without any essential loss of accuracy only the first mode in the cross-flow direction, y, was retained in all cases (i.e. $n = 1$). Several modes in the flow direction, x, were included to determine modal convergence (i.e. $m = 1, 2, \dots 12$). Figure 2 shows the assumed membrane mode shapes for the "SSSF" case, the satisfaction of the geometric boundary conditions can be noted, where the leading and side edges of the structure have zero out-of-plane displacement.

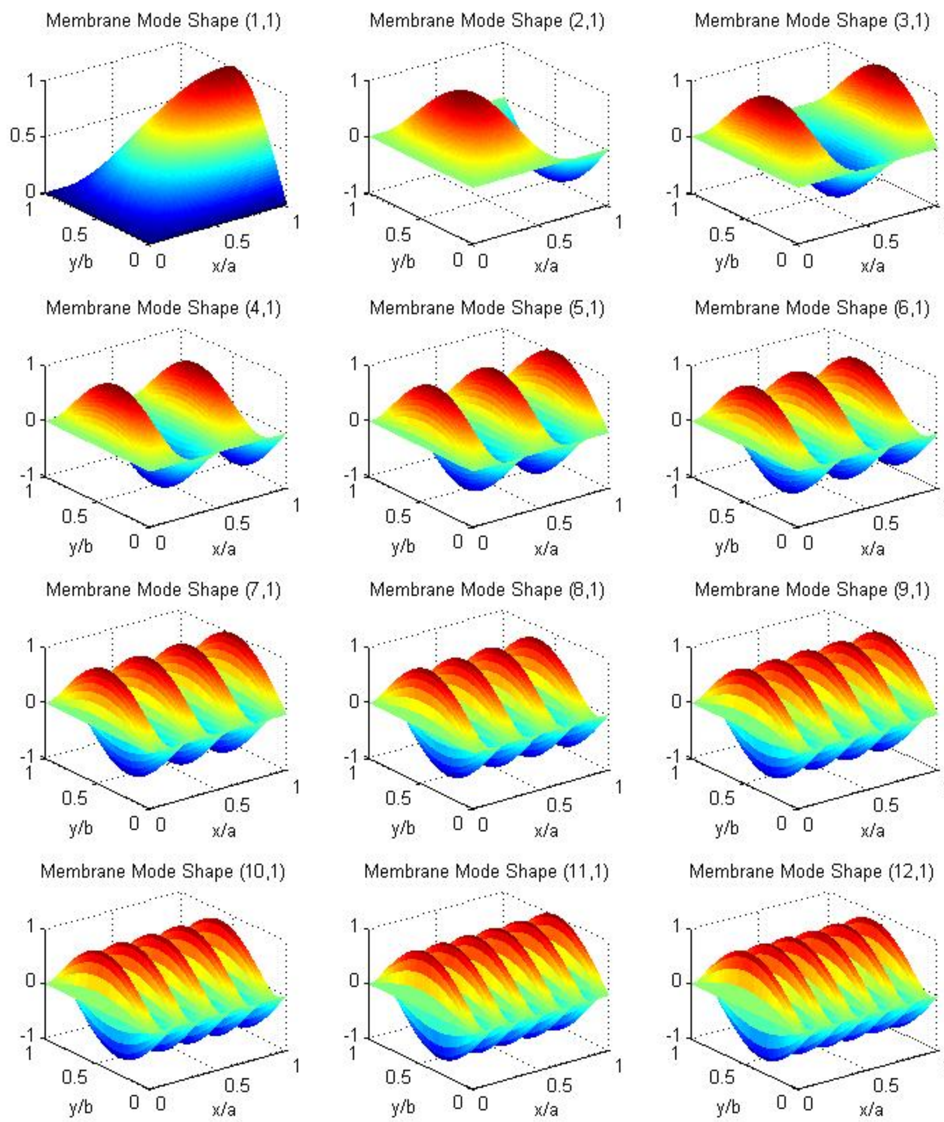

Figure 2 Assumed mode shapes for simply supported plate with leading and side-edges fixed, trailing edge free boundary conditions

2.3.2. Plate Modes

The membrane mode shapes described in the previous section may not fully capture the influence of the boundary conditions on the dynamic behavior of a plate. Further, they do not fully satisfy the boundary conditions of the plate model. Plate modes, or two dimensional products of one-dimensional beam modes, which include the effect of the clamped boundary condition at the fixed edges of the structure were thus also considered in the study. At the fixed boundaries, the clamped boundary condition requires that both the out-of-plane displacement of the structure be zero, like that of the membrane modes, and the slope of the structure's out-of-plane displacement be zero at that boundary as well. As with the membrane modes, two boundary condition configurations were considered and are described below.

Configuration 3. CCCC

The first case is again with all edges fixed, this time with a clamped boundary condition. The abbreviation for the configuration in future discussion is "CCCC". To obtain the clamped-clamped beam mode shape for each direction in this case, the second derivative of the free-free beam mode shape provided by Dowell (16) was computed and used and is shown below.

$$\boldsymbol{\widetilde{\Psi}_n(\widetilde{y}) = \frac{\cos B_n - \cosh B_n}{\sinh B_n - \sin B_n}(\sinh B_n\widetilde{y} + \sin B_n\widetilde{y}) + (\cosh B_n\widetilde{y} - \cos B_n\widetilde{y})} \qquad (2.41\text{ a-b})$$

$$B_n \to (2n+1)\frac{\pi}{2}$$

The exact coefficient, B_n, values for the first modes of the clamped-clamped mode shape was obtained by considering the generalized form of the beam equation as presented by Bisplinghoff et. al. (17) as equation (3-29) and reproduced here.

$$\boldsymbol{W = C\sinh\sqrt{\frac{\omega}{a}}y + D\cosh\sqrt{\frac{\omega}{a}}y + E\sin\sqrt{\frac{\omega}{a}}y + F\cos\sqrt{\frac{\omega}{a}}y} \qquad (2.42)$$

where,

$$\boldsymbol{a^2 = \frac{EI}{m}} \qquad (2.43)$$

The unknowns in this equation include the coefficients and the natural frequency, ω. Using the boundary conditions to determine the coefficients C, D, E, and F, we will solve for the natural frequencies.

The boundary conditions of the clamped-clamped beam require that the displacement and slope at the end points be zero.

$$\begin{aligned} \boldsymbol{W(0)} &= \boldsymbol{0} \\ \boldsymbol{W'(0)} &= \boldsymbol{0} \\ \boldsymbol{W(b)} &= \boldsymbol{0} \\ \boldsymbol{W'(b)} &= \boldsymbol{0} \end{aligned} \qquad (2.44\text{ a-d})$$

Applying equation (**2.42**) to each of equations (**2.44** a-d) gives four equations with four unknown coefficients as follows.

$$\begin{aligned} \boldsymbol{W(0)} &= \boldsymbol{0 = D + E} \\ \boldsymbol{W'(0)} &= \boldsymbol{0 = C + F} \\ \boldsymbol{W(b)} &= \boldsymbol{0 = C\sinh\sqrt{\frac{\omega}{a}}b + D\cosh\sqrt{\frac{\omega}{a}}b + E\sin\sqrt{\frac{\omega}{a}}b + F\cos\sqrt{\frac{\omega}{a}}b} \end{aligned} \qquad (2.45\text{ a-d})$$

$$\boldsymbol{W'(b) = 0 = C\cosh\sqrt{\frac{\omega}{a}}y + D\sinh\sqrt{\frac{\omega}{a}}y + E\cos\sqrt{\frac{\omega}{a}}y - F\sin\sqrt{\frac{\omega}{a}}y}$$

The four equations can be simplified to a single expression in terms of one coefficient, in this case we've chosen D, the following equation results.

$$\boldsymbol{0 = D\left[\frac{\left(\cos\sqrt{\frac{\omega}{a}}b - \cosh\sqrt{\frac{\omega}{a}}b\right)}{\left(\sinh\sqrt{\frac{\omega}{a}}y - \sin\sqrt{\frac{\omega}{a}}y\right)} + \frac{\left(\sinh\sqrt{\frac{\omega}{a}}y + \sin\sqrt{\frac{\omega}{a}}y\right)}{\left(\cosh\sqrt{\frac{\omega}{a}}b - \cos\sqrt{\frac{\omega}{a}}b\right)}\right]} \tag{2.46}$$

Letting the coefficient be identically zero, i.e. $D \equiv 0$, gives a trivial solution. Therefore, the rest of the equation must be identically zero and we can solve for the remaining unknown, the frequencies, ω, that make that true. To find those frequencies, it is helpful to first simplify the analytical expression, the following transcendental equation results.

$$\boldsymbol{\cos\sqrt{\frac{\omega}{a}}b = \frac{1}{\cosh\sqrt{\frac{\omega}{a}}b}} \tag{2.47}$$

Each side of equation (**2.47**) can be plotted graphically. Where the two functions intersect gives the values of the frequencies of interest which will appear in the form $B_n\pi$.

Analysis of the resulting frequency values shows that the frequencies determined by this method are well approximated using the analytical expression for the coefficient of the free-free beam mode given by equation (**2.41** a-b).

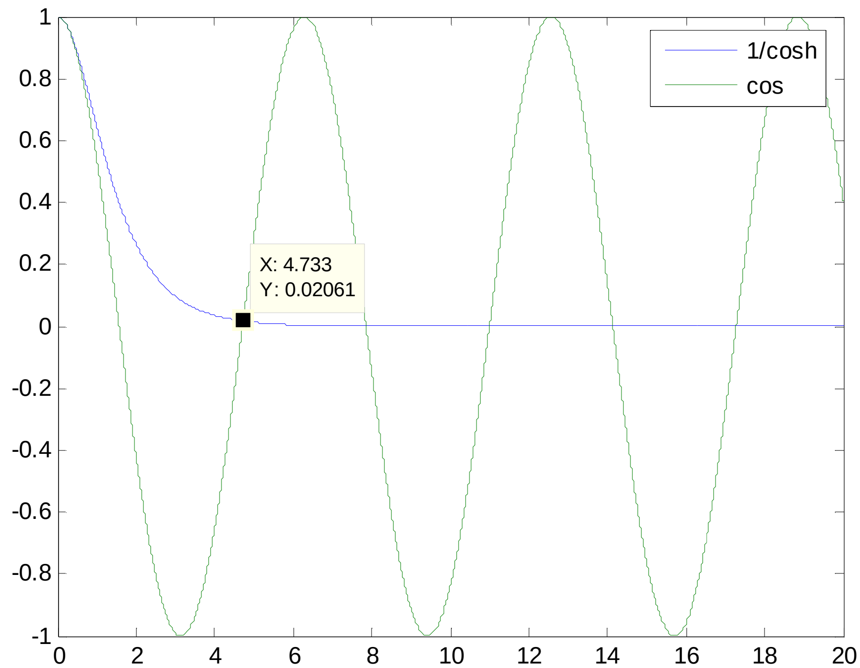

Figure 3 Graphical solution of the transcendental equation for the clamped-clamped beam

An approximate form can also be used for the higher mode shapes. As presented by Dowell (16), the approximation is very good for higher modes and was used for $m \geq 4$. The approximate shape is as follows, the coefficients, B_n are as previously stated above.

$$\boldsymbol{\widetilde{\Psi}_m(\widetilde{x}) = -\sin B_m\widetilde{x} + \cos B_m\widetilde{x} + e^{-B_m\widetilde{x}} - (-1)^m e^{-B_m(1-\widetilde{x})}} \qquad (2.48)$$

As with the simply supported cases, only one mode was used in the cross-flow direction to complete the analysis, while again, several modes were included in the flow direction to demonstrate convergence.

Configuration 4. CCCF

The second configuration for the plate modes has three fixed boundary conditions, the two side edges, and the leading edge, while the trailing edge remains free. The abbreviation for this case in future discussion is "CCCF".

For the first three modes in the flow direction, x, which will be represented by a clamped-free beam mode, the exact expression for the mode shape was used.

$$\boldsymbol{\widetilde{\Psi}_m(\widetilde{x}) = \frac{\sin B_m - \sinh B_m}{\cosh B_m - \cos B_m}(\sinh B_m\widetilde{x} - \sin B_m\widetilde{x}) + (\cosh B_m\widetilde{x} - \cos B_m\widetilde{x})}$$

$$\boldsymbol{B_1 = 0.551\pi} \qquad (2.49 \text{ a-d})$$

$$\boldsymbol{B_2 = 1.49\pi}$$

$$B_m \to (2m-1)\frac{\pi}{2}$$

The coefficient, B_m, of the argument of the terms in the non-dimensional cantilevered beam equation shown are obtained from the literature, but were calculated exactly by the method previously described for the clamped-clamped beam mode configuration (17). For higher modes, $m \geq 3$, the exact value is well approximated by the analytical expression for the coefficient.

A further approximation to the higher modes shapes can also be made. Additional modes, $m \geq 4$, were approximated using the asymptotic approximation formula provided by Dowell (16).

$$\boldsymbol{\widetilde{\Psi}_m(\widetilde{x}) = \sin B_m\widetilde{x} - \cos B_m\widetilde{x} + e^{-B_m\widetilde{x}} + (-1)^{m+1}e^{-B_m(1-\widetilde{x})}} \qquad (2.50)$$

In the cross-flow direction, y, the clamped-clamped beam mode was applied. This mode shape was described in Case 1 and will not be reproduced here. Because only the first mode was applied in this direction, only the exact mode was used.

The plate mode shapes that have just been described can be represented graphically as shown in Figure 4. The most notable difference between the membrane and beam modes occurs at the boundaries where the differences between the simply-supported and clamped conditions are manifest. In the case of the clamped boundary conditions, the leading and side-edges are not only fixed, but have a zero degree slope at those boundaries. The trailing edge also exhibits a slightly revised shape with less curvature in the plate modes than the membrane modes. This is harder to discern in the figures.

We have now concluded the theoretical discussion of the structural model and its modal components. Before we can explore the results of our calculations however, we must now turn our attention to the aerodynamic forcing term and its derivation.

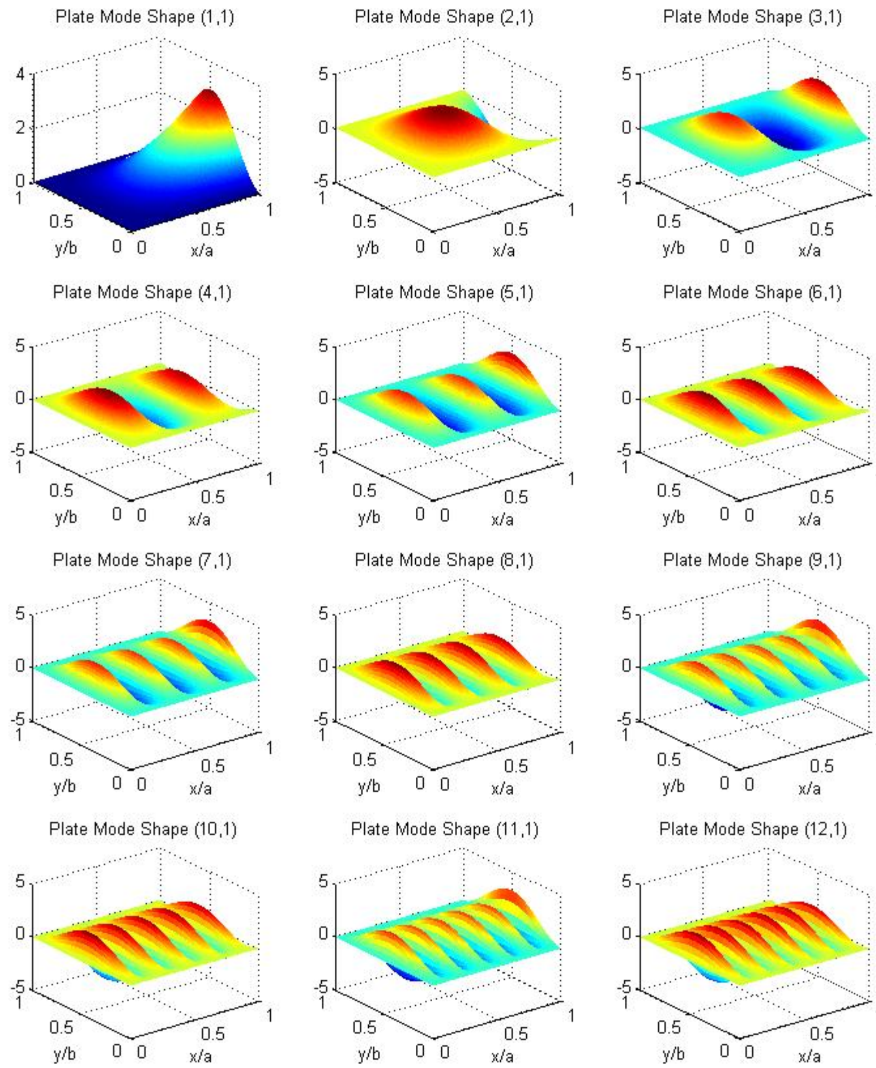

Figure 4 Assumed mode shapes for a clamped plate with leading and side-edges fixed, trailing edge free boundary conditions

3. Aerodynamic Model

We now turn our attention to the pressure, or forcing term. As previously alluded to in the non-dimensional description of the full equation of motion, the forcing term can be written as follows.

$$\boldsymbol{\tilde{Q}_{kl}} = \iint \frac{\boldsymbol{\Delta p}}{\boldsymbol{\rho U_\infty^2}} \boldsymbol{\tilde{\Psi}_{kl} d\tilde{x} d\tilde{y}} \tag{3.1}$$

The pressures forces acting on the structure are due to fluctuations in the flow field. Potential flow theory is used to describe the flow field of interest here where the assumptions of classic aerodynamics apply, i.e. that the flow be linear, isentropic, inviscid and irrotational. The governing field equation can be stated as follows, where the ϕ is the perturbation velocity potential (12).

$$\boldsymbol{\nabla^2 \phi - \frac{1}{a_\infty^2}\left[\frac{\partial}{\partial t} + U_\infty \frac{\partial}{\partial x}\right]^2 \phi = 0} \tag{3.2}$$

The equation relating the velocity potential and the pressure is known as Bernoulli's equation, here linearized about a uniform mean flow condition.

$$\boldsymbol{p_\pm = -\rho\left[\frac{\partial \phi}{\partial t} + U_\infty \frac{\partial \phi}{\partial x}\right]_{z=0\pm}} \tag{3.3}$$

The pressure will be evaluated at $z = 0 \pm$ in keeping with the approximations of linear theory. Because flow will pass on both sides of the structure, the pressure differential across the structure is required, simply $\Delta p = p_+ - p_-$.

Finally, the boundary conditions are required. For the configuration considered here, there are two conditions, one on the structure, and one off.

$$\left.\frac{\partial \phi}{\partial z}\right|_{z=0\pm} = \frac{\partial w}{\partial t} + U_\infty \frac{\partial w}{\partial x}$$
$$\left.\frac{\partial \phi}{\partial z}\right|_{z=0\pm} = 0 \qquad (3.4\text{ a-b})$$

On the structure, the out-of-plane velocity of the flow must be equal to that of the structure, this is expressed mathematically in equation (**3.4** a-b). Off of the structure, the out-of-plane velocity must be zero. This condition is being enforced by the presence of the baffle assumed to hold the structure and be infinite in extent. In the far field, an additional condition of finiteness is also imposed on the solution as $z \to \infty$.

Following the development first presented by Dowell (18), the resulting solution for the pressure can be efficiently expressed in the form of the generalized aerodynamic force, Q_{mnkl}, here shown in the non-dimensional form used in the calculations.

$$\begin{aligned}\tilde{Q}_{mnkl} &= \tilde{q}_{mn}(s)\tilde{S}_{mnkl} + \dot{\tilde{q}}_{mn}(s)\tilde{D}_{mnkl} \\ &\quad + \int_0^{\tau}\left[\tilde{q}_{mn}(\tau)\tilde{H}_{mnkl}(s-\tau) + \dot{\tilde{q}}_{mn}(\tau)\tilde{I}_{mnkl}(s-\tau)\right]d\tau\end{aligned} \qquad (3.5)$$

where,

$$\tilde{S}_{mnkl} \equiv \frac{1}{M}\int_0^1\int_0^1 \frac{\partial \tilde{\Psi}_{mn}}{\partial \tilde{x}}\tilde{\Psi}_{kl}\,d\tilde{x}\,d\tilde{y}$$

$$\tilde{D}_{mnkl} \equiv \frac{1}{M}\frac{1}{U_\infty}\int_0^1\int_0^1 \tilde{\Psi}_{mn}\tilde{\Psi}_{kl}\,d\tilde{x}\,d\tilde{y} \qquad (3.6\text{ a-e})$$

$$\begin{aligned}\tilde{H}_{mnkl}(s) &= -\frac{1}{4\pi^2}\frac{U_\infty}{M^2}\int\int_{-\infty}^{\infty}\tilde{G}_{mnkl}\,i\tilde{\alpha}\Bigg[\tilde{\alpha}^2 \\ &\quad + \tilde{\gamma}^2\left(\frac{a}{b}\right)^2\Bigg]^{\frac{1}{2}}\exp[-i\tilde{\alpha}s]\,J_1\left[\left(\tilde{\alpha}^2 + \tilde{\gamma}^2\left(\frac{a}{b}\right)^2\right)^{\frac{1}{2}}\frac{s}{M}\right]d\tilde{\alpha}\,d\tilde{\gamma}\end{aligned}$$

$$\boldsymbol{I_{mnkl}(s) = -\frac{1}{4\pi^2}\frac{1}{M^2}\int\int_{-\infty}^{\infty}\tilde{G}_{mnkl}\left[\tilde{\alpha}^2 + \tilde{\gamma}^2\left(\frac{a}{b}\right)^2\right]^{\frac{1}{2}}\exp[-i\tilde{\alpha}s]\,J_1\left[\left(\tilde{\alpha}^2 + \tilde{\gamma}^2\left(\frac{a}{b}\right)^2\right)^{\frac{1}{2}}\frac{s}{M}\right]d\tilde{\alpha}d\tilde{\gamma}}$$

$$\boldsymbol{G_{mnkl} \equiv \int_0^1\int_0^1\tilde{\Psi}_{mn}(\tilde{x},\tilde{y})e^{-i\tilde{\alpha}\tilde{x}-i\tilde{\gamma}\tilde{y}}d\tilde{x}d\tilde{y}\int_0^1\int_0^1\tilde{\Psi}_{kl}(\tilde{x},\tilde{y})e^{i\tilde{\alpha}\tilde{x}+i\tilde{\gamma}\tilde{y}}d\tilde{x}d\tilde{y}}$$

The first two terms, S_{mnkl} and D_{mnkl}, are considered the piston theory terms, and they dominate in the super-sonic flow regimes when the influence of behavior at previous times in the flow diminishes. Piston theory describes the forces acting perpendicular to the plate, or in the piston of fluid extending in the out-of-plane direction from the structure. The next two terms, the influence functions, H_{mnkl} and I_{mnkl}, account for the influence of the flow field at previous times on the current instant of time. They are most pronounced in sub-sonic flow, the flow regime of interest in this study. The influence functions are computed numerically and stored, while analytical expressions for the piston terms are available.

4. Parameter Study

Three cases of model and mode shape combinations were studied however only two systems are presented herein. The modal configurations were described in the last section and the three model-mode shape systems are described below.

- Membrane-Membrane (M-M): membrane model (tension terms included, no stiffness terms) with membrane modes. Results from this system are not included herein due to inconclusive convergence and behavior patterns. Additional analysis is required to determine the full effect of tension on the systems.
- System 1. Simply Supported Plate: plate model with membrane modes, represents simply supported boundary conditions, two configurations, Case 1 SSSS, Case 2 SSSF
- System 2: Clamped Plate: plate model with plate modes, represents clamped boundary conditions, two configurations, Case 3 CCCC, Case 4 CCCF

In each system and configuration, a parameter study was undertaken in which several parameters were held fixed during the entirety of the computations and others were varied to determine behavior and achieve convergence.

4.1. Parameters

4.1.1. Structural Parameters

The structural parameters are largely comprised of the physical extent of the structure. Again, these parameters were set by an experimental apparatus that was designed for the Duke University wind-tunnel. The baffle holds a structural sample approximately 0.3 m by 0.2 m in the flow and cross-flow directions respectively. Thus, the coordinate lengths are $a = 0.3$, and $b = 0.2$, for a fixed structural ratio of $\frac{a}{b} = 1.5$. Results are compared to published findings for the all edges simply supported (SSSS) case for structural ratios of $\frac{a}{b} = 0$ and $\frac{a}{b} = 1.0$.

In addition, to maintain the numerical stability of the calculations a small amount of empirical damping was included in the structural model. The value of the damping coefficient, ζ, was determined using the homogenous (no forcing) form of the equation of motion, Equation (2.35). For the simply supported system, Cases 1 SSSS and 2 SSSF, the damping coefficient $\zeta = 0.02$. This suppressed numerically divergent behavior in all twelve modes in both cases. For the clamped system, Cases 3 CCCC and 4 CCCF, the damping coefficient $\zeta = 0.09$. This value suppressed numerically divergent behavior for all twelve modes in Case 3 CCCC, however a higher damping coefficient of $\zeta = 0.19$ was required to do so for Case 4 CCCF. For the purposes of comparison, it was determined that the former value would be used in all clamped system calculations.

4.1.2. Material Properties

For the implementation of the proposed noise reducing structure in a real aircraft material selection will be a key factor. Engineers at NASA Langley Research Center (LaRC) experimented with several materials and provided the author with samples of several elastomeric materials under consideration. To complete the calculations, the stiffest and thickest sample was used to generate the material properties.

To determine the Young's modulus, E, of the elastomeric materials, NASA engineer Ji Su performed tension tests on several samples at a lab at NASA LaRC. An average value of the nine reported tests was used in the calculations giving a Young's modulus of $E = 1.84e6$ Pa. This value is derived from a relatively small number of samples, especially considering the high variability in the testing results reflected in the fact that the standard deviation on the average value reported is on the order of 50 percent. Although this should be noted when comparing the computed results presented herein to experiments using the material, the non-dimensionalization of the results should render the issue moot.

Additional parameters measured from samples of the elastomeric material include the thickness which was measured at $h = 0.001753$ m. Using the thickness, a density could also be determined, $\rho = 1230$ kg/m^3. Finally, the Poisson's ratio was assumed to be $\nu = 0.5$ based on Wikipedia estimates for rubber materials (19).

Additional parameters appearing in the calculations, like stiffness, D, were calculated from the values presented above.

4.1.3. Mach Number

The primary interest of this study is sub-sonic flow regimes that are representative of landing configuration flow fields. As such, a reference Mach number was chosen such that it fell within these bounds and was also within the capabilities of the Duke wind-tunnel in which experimental verification of the computed results is intended to take place. For all cases and configurations, calculations were completed at Mach = 0.1. Additional mach number are included in the following table for reference and discussion purposes.

Table 1 Mach Numbers, M, and Corresponding Flow Speeds, U, used in study (assumes speed of sound at STP, $a_\infty = 343$ m/s)

	Flow Speed, U	
Mach Number, M	m/s	mph
0.05	17.15	38.4
0.1	34.3	76.7
0.15	51.45	115.1

4.1.4. Altitude

To determine the stability or instability of the structure from its time-history, the altitude of the flow field was adjusted over a wide range. Adjusting the altitude means adjusting the density of the flow, ρ, and the speed of sound, a_∞. The values used in the calculations were obtained from the literature (20).

Table 2 Summary of sample altitude data used in calculations

Parameter	*English Units*				
Height above Sea Level, h	**ft**	**0**	**4000**	**8000**	**10000**
Temperature, t	**degree F**	59	44.47	30.49	23.36
Speed of Sound, a	**ft/s**	1117	1102	1086	1078
Pressure, p	**lbf/ft^2**	2116.2	1827.7	1571.9	1455.4
Mass Density, ρ	**slug/ft^3**	0.002378	0.002112	0.001869	0.001756
Coef. Of Viscosity, ν x 10^7	**slug/ft sec**	3.719	3.639	3.557	3.515
Parameter	*Metric Units*				
Height above Sea Level, h	**m**	0	1219.2	2438.4	3048
Temperature, t	**degree C**	15	6.93	-0.84	-4.80
Speed of Sound, a	**m/s**	**340.5**	**335.9**	**331.0**	**328.6**
Pressure, p	**N/m^2**	101324.2	87510.7	75263.0	69684.9
Mass Density, ρ	**kg/m^3**	**1.226**	**1.088**	**0.963**	**0.905**
Coef. Of Viscosity, ν x 10^7	**Pa s**	178.1	174.2	170.3	168.3

In cases where the desired altitude was required but not contained in the tables explicitly, a quadratic curve fit was developed and used to determine the value of interest for mass density, and a linear curve fit was used to calculate the speed of sound.

It is of note that once the altitude reaches a certain point, above 40-50,000 ft, the density has diminished to such an extent that the curve fit will eventually go negative, and the speed of sound has stopped changing. It is possible, that at these high altitudes the assumptions of the model used to make the tabulated calculations presented in the literature breaks down. Using the nominal structural and material properties, several calculations required use of altitude data well above 50,000 ft, where the extrapolated data is weakest. To address this limitation and achieve a more reasonable non-dimensional result, the thickness of the structure was adjusted using a thickness factor,

h_f, applied to the nominal thickness. As a result, lower altitudes with correspondingly higher air mass densities and speeds of sound in the linear range resulted in the identification of the stability or flutter boundary.

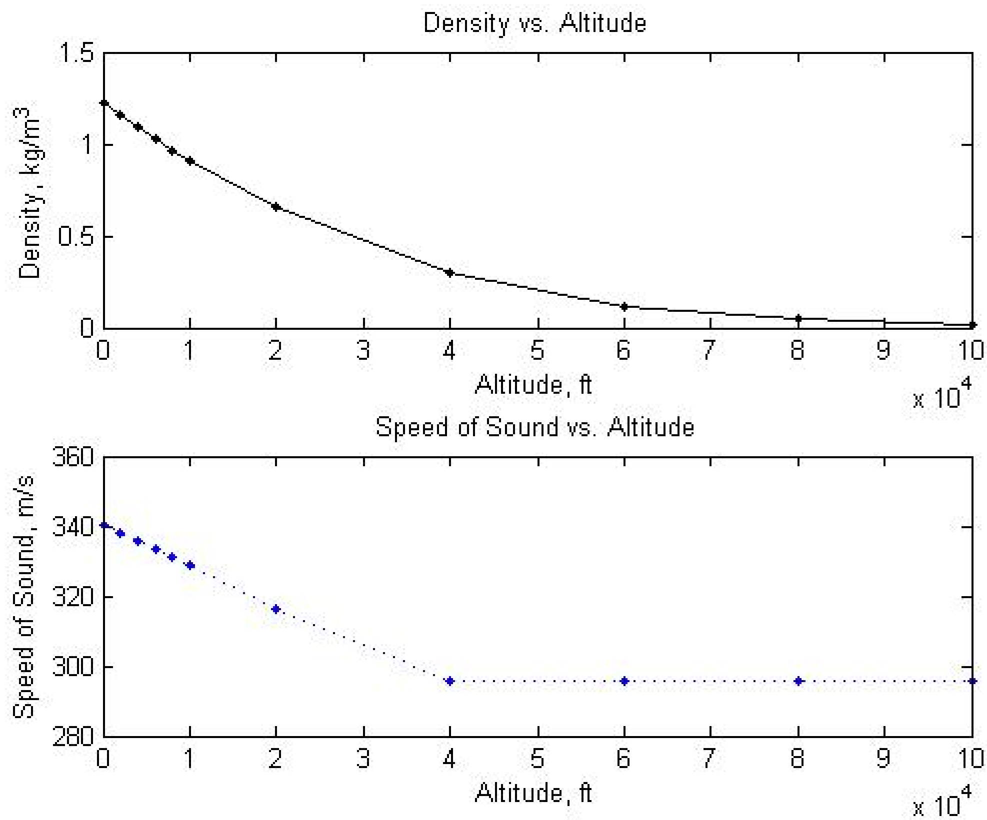

Figure 5 Air mass density from tabulated values plotted with extrapolation curves

4.1.5. Number of Modes

To verify the accuracy of the result, additional modes are successively included in the calculations. Once the dominant modes are included in the computational model, additional modes should serve only to refine the resulting behavior and not have a significant effect. This assumes that the low modes are indeed driving the behavior and the higher modes are not as important. It is always possible that adding more modes will result in the discovery of an additional dominant mode, however due to limited time and resources, a reasonable stopping point must be determined. In the case of the calculations presented herein, the inclusion of at least two additional modes with clear asymptotic convergence of the resulting flutter boundary was determined to be sufficient.

4.2. Flutter Boundary

From the time marching calculations conducted for each parameter set, one of three behaviors were observed. Each of the three behaviors is shown below using representative plots of time history and frequency content. The frequency plots are generated by taking a Fast Fourier Transform (FFT) of the time history in MATLAB. All the plots are from cases run for the SSSF configuration, $h_f = 3$, altitudes of 20,000 ft for one mode, 17,000 ft for two modes and 20,000 ft for eight modes for the damped, diverging and flutter behaviors respectively.

Oscillating Damped Decay: The first behavior, oscillating, damped decay is a stable behavior.

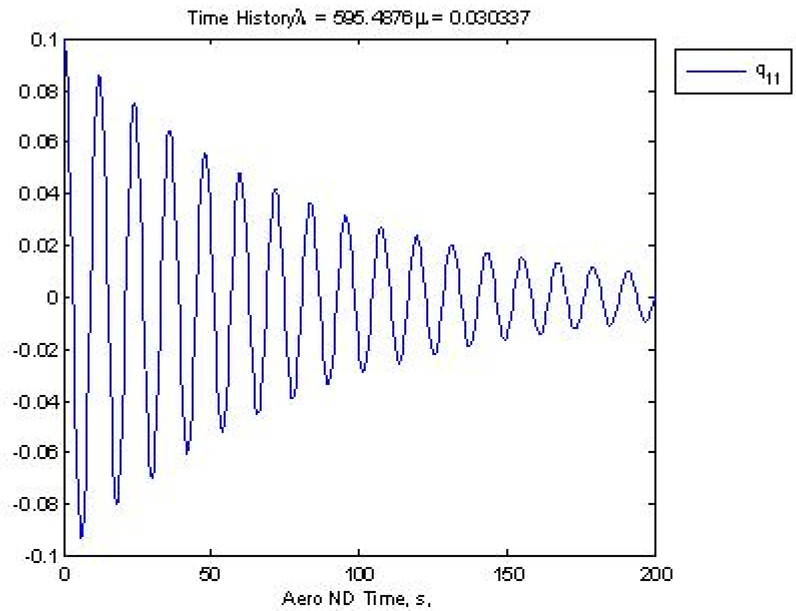

Figure 6 Time history showing damped oscillating decay: 20,000 ft altitude for one mode

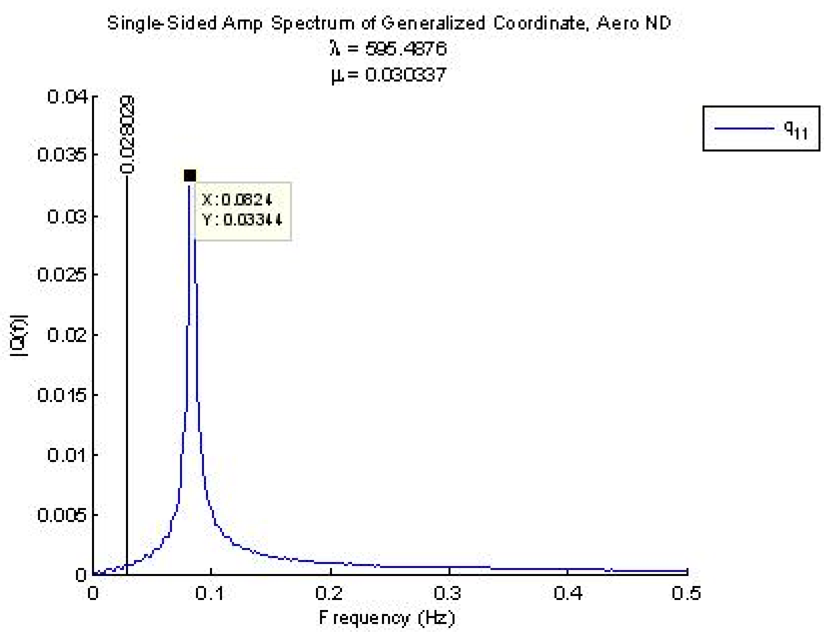

Figure 7 FFT of time history for damped oscillating decay: 20,000 ft altitude for one mode

The time history for one mode and the corresponding FFT showing the frequency content are shown in Figure 6 and Figure 7 respectively. In this case, the structural stiffness is able to overcome the influence of the aerodynamic forcing and the aeroelastic system returns to a stable equilibrium.

Divergence: Divergence is characterized by an unstable and exponential escape of the generalized coordinate. There is no oscillation evident, so no frequency content, and the implied instability of the structure is severe.

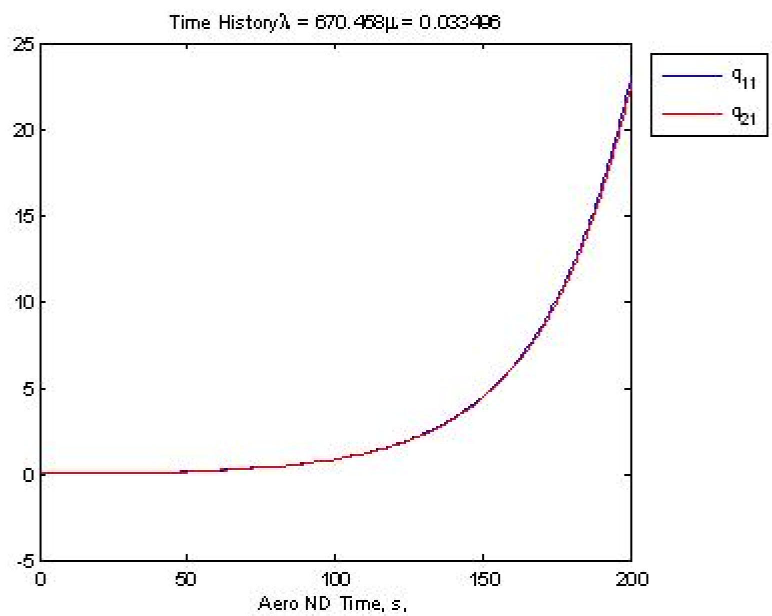

Figure 8 Time history showing divergence: 17,000 ft altitude for two modes

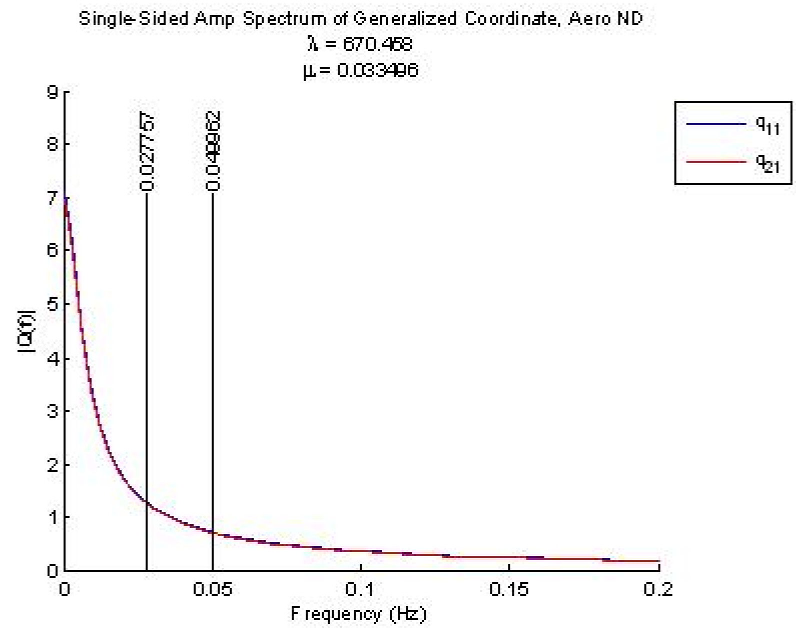

Figure 9 FFT of time history for divergence: 17,000 ft altitude for two modes

Flutter: Finally, flutter is also an unstable behavior, and like divergence, it escapes exponentially, however it also shows oscillations as it does so.

Flutter per sea by definition is a linear phenomenon. In the presence of non-linear effects, however, it is possible to see oscillations that grow to a finite amplitude. This phenomenon is known as Limit Cycle Oscillations (LCO). Since non-linear effects are not included in the model used herein, the amplitude of the oscillating instability continues to grow unchecked. It should be noted that while it is not possible to see LCO behavior in the modeled results, the behavior may be present in the physical system.

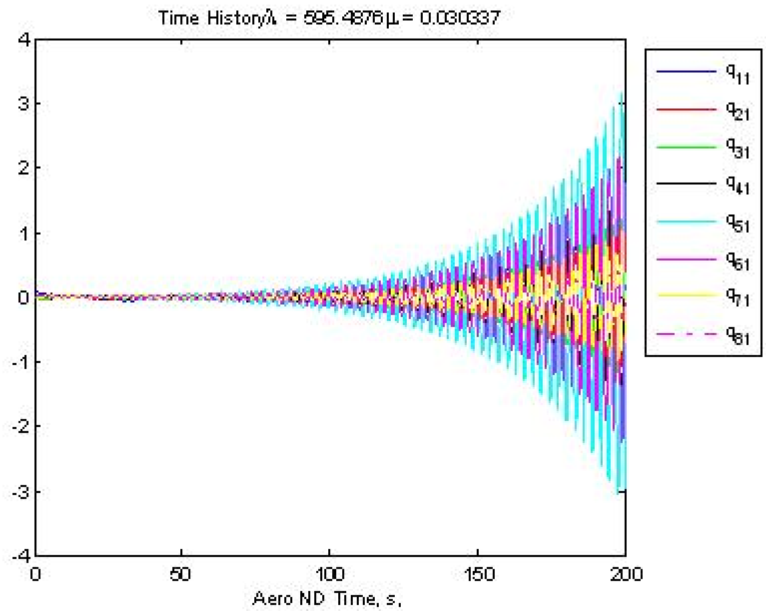

Figure 10 Time history showing flutter: 20,000 ft altitude for eight modes

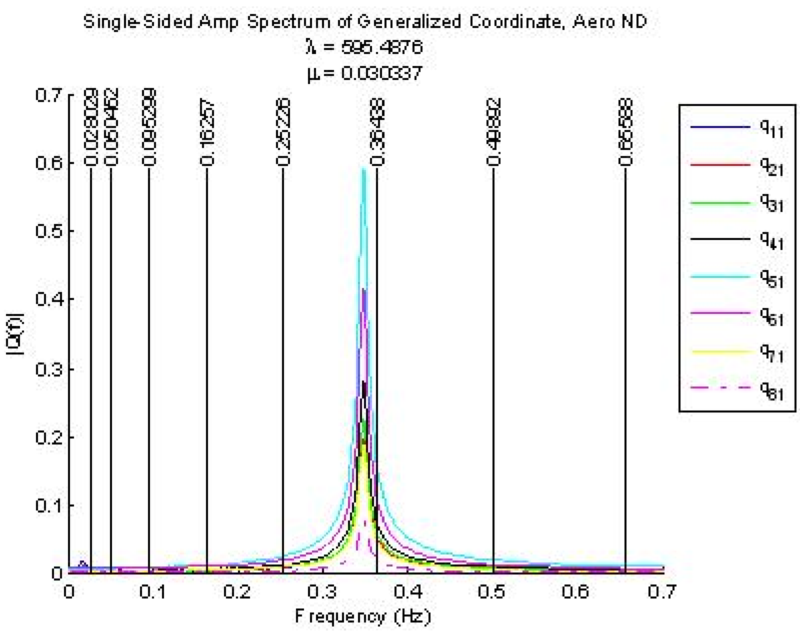

Figure 11 FFT of time history for flutter: 20,000 ft altitude for eight modes

Several additional details can be observed from Figure 11. The vertical lines in the plot indicate natural frequency values. The width and height of the frequency peaks also indicate the mode driving the unstable behavior and at what frequency. In the case shown in Figure 11, the fifth and sixth modes appear to be driving the flutter at close to the sixth mode natural frequency.

To determine the flutter boundary, the study seeks to find the set or range of parameters between which the recorded time history switches from the stable to an unstable behavior. This is recorded as the flutter boundary and shown in the results plotted against the non-dimensional dynamic pressure, λ, a ratio of the aerodynamic and structural forces in the system.

4.3. Method

The flutter boundary results, as well as the natural frequency calculations presented herein were obtained from a time-marching code developed by the author in the MATLAB programming language. The aerodynamic influence functions, H_{mnkl} and I_{mnkl}, required to complete the time marching analysis were calculated using a series of codes, one for each mode. In addition, several integration computations, for instance to determine the stiffness and mass matrices, were completed in Mathematica™ and imported to the time marching code for further manipulation. The code and work books used to make these calculations are not included here.

5. Computational Results

Computational results will be presented in two cases previously described in Chapter 4, they are: System 1. Simply Supported Plate Model, and System 2. Clamped Plate Model. Each case summary presented herein will address the computed natural frequency, the flutter boundary from time-history data, and modal convergence of the results.

5.1. System 1: Simply Supported Plate Model

5.1.1. Natural Frequency

The natural frequencies for the two simply supported configurations presented herein are summarized in Figure 12. The natural frequencies of Case 2 SSSF, with the free trailing edge, are lower than Case 1 SSSS in which all edges are fixed. All natural frequencies presented are decoupled so including additional modes does not result in a change or convergence of the resulting values. It should be noted that the natural frequencies presented are distinct; the lines connecting the values are to facilitate visualization of differences between the two cases.

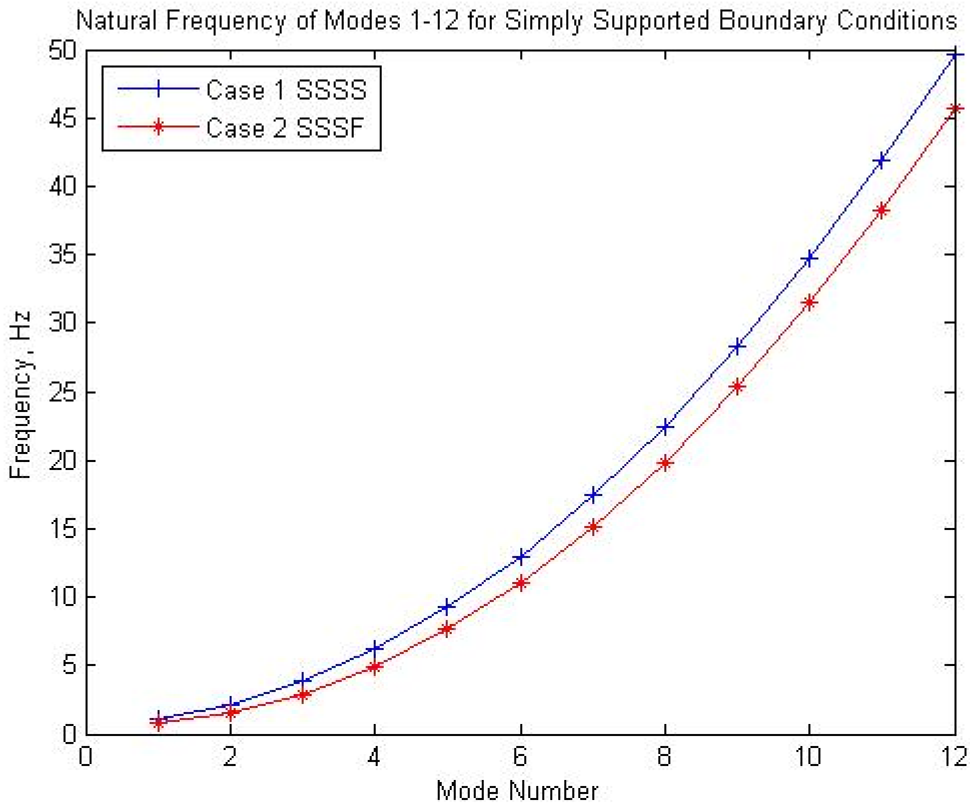

Figure 12 Natural frequency of modes 1-12 for simply supported boundary condition cases

5.1.2. Flutter (and Divergence inter alia) Calculations

The convergence of the flutter or divergence dynamic pressure boundary is presented in Figure 13. Below the flutter or divergence boundary, time history calculations result in stable behavior usually manifest as damped oscillations. Above the flutter or divergence boundary, the plate behavior is unstable, resulting in either divergence or flutter behavior as previously described.

Case 1 SSSS shows rapid convergence of the flutter boundary. Only two or three modes are required to reach a stable boundary exhibiting little change with additional modes suggesting the first and/or second mode is driving the instability. The frequency content of the flutter behavior indicates a combination of the first and second modes driving the instability. The unstable behavior calculated with only one mode shows divergence. Additional modes lead to unstable behavior showing flutter. The low number of modes required to achieve convergence is consistent with results found in the literature (12).

Case 2 SSSF takes three times as many modes to reach a converged flutter boundary. Time histories of the plate behavior show the flutter driven by the fifth and sixth modes which have the largest amplitude and drive the frequency. This behavior holds with up to 12 modes included in the calculation. When only one mode is included in the calculation, the behavior is inherently stable, therefore no flutter point is shown for the one mode calculation. When fewer than five modes are included, the unstable flutter behavior is driven by the first mode, but the flutter boundary shifts as more modes are included and the boundary does not converge until more modes are included. The number of modes needed to achieve convergence is much higher than for Case 1 SSSS, and the modes driving the instability are also much higher than for that configuration.

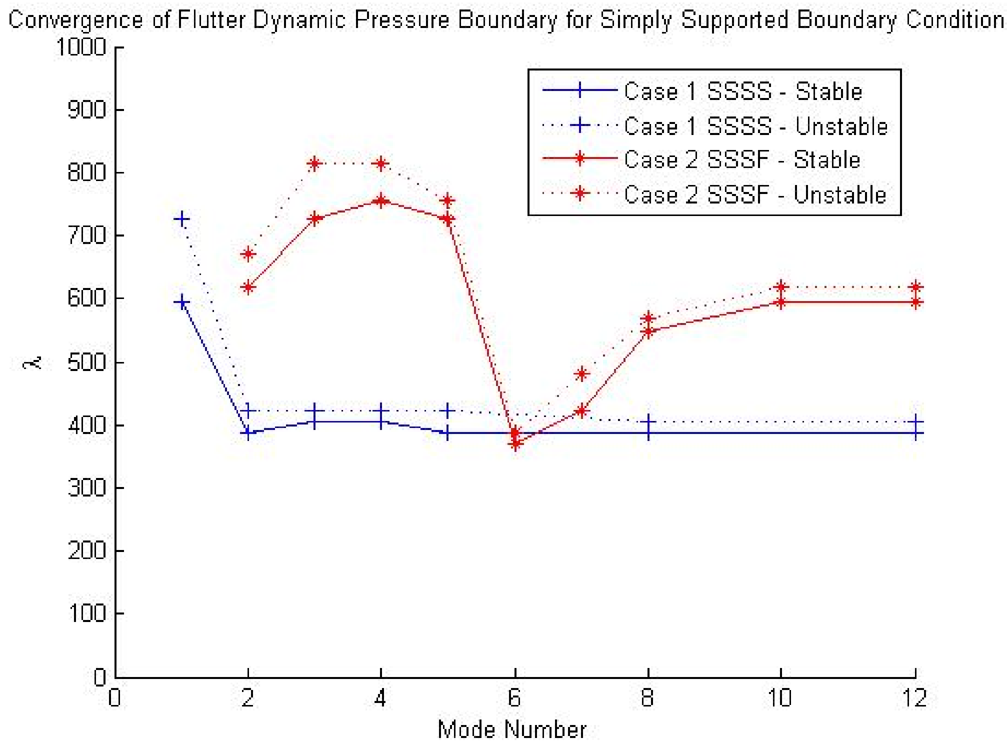

Figure 13 Convergence of flutter dynamic pressure boundary for simply supported boundary condition cases

5.1.3. Convergence

The flutter or divergence boundary is considered converged when both the dynamic pressure and the flutter frequency are no longer changing with the inclusion of additional modes in the calculation.

As previously mentioned, Case 1 SSSS converges rapidly with only two or three modes included in the calculation. Figure 14 shows this convergence behavior. It also shows that the two modal frequencies exhibited by the unstable system track but are slightly lower than the first and second natural frequencies leading to the conclusion that these two modes are dominating the behavior.

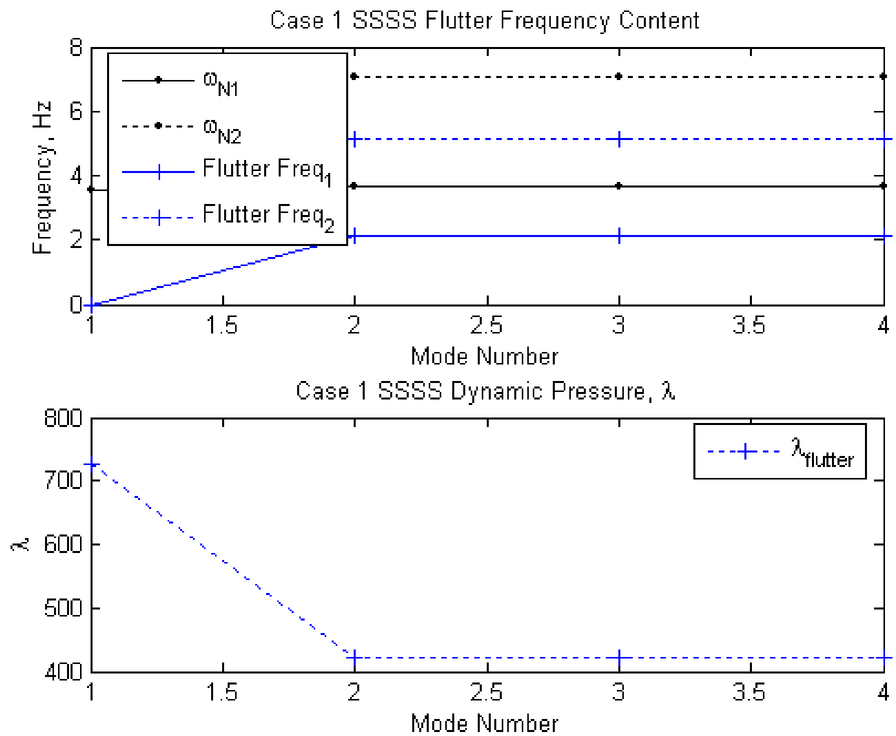

Figure 14 Flutter frequency convergence and dominant mode identification for Case 1 SSSS

In contrast, Case 2 SSSF takes a much larger number of modes to converge and does so in a much higher modal combination. Figure 15 shows this convergence of both the dynamic pressure and the frequency content of the unstable behavior for Case 2 SSSF. By the time all 12 modes are included, as shown, the two indicators seem to have converged. Again, a combination of modes, in this case the fifth (frequency not shown) and the sixth modes (frequency shown) are combining to dominate the unstable behavior when a large number of modes are included in the calculation. Modal amplitude data was also used to make this determination.

While the frequency content appears converged with fewer than six modes, the dynamic pressure boundary has not stabilized which is further confirmation that both parameters must be taken into account in determining convergence.

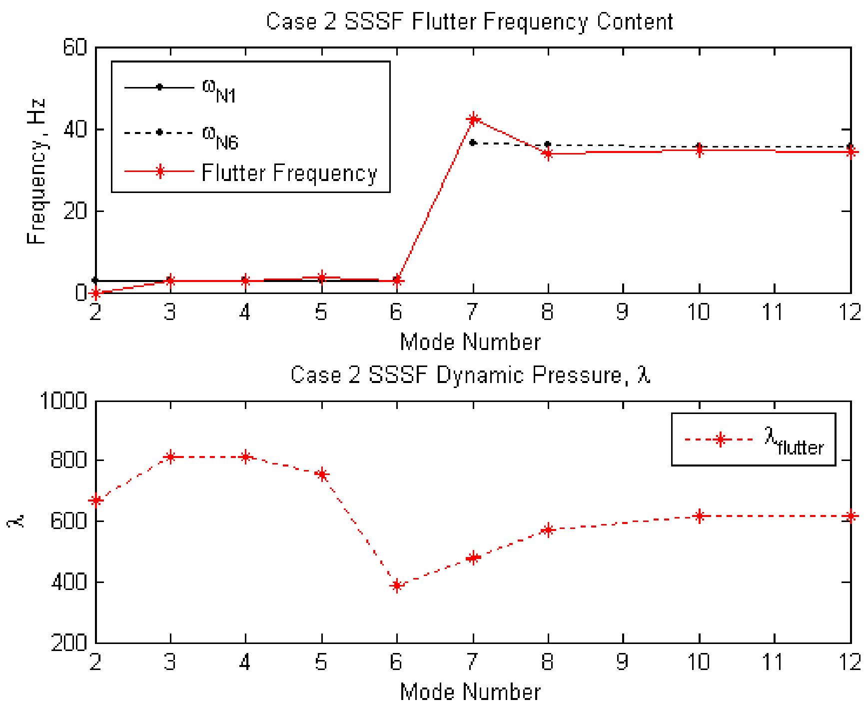

Figure 15 Flutter frequency convergence and dominant mode identification for Case 2 SSSF

5.1.4. Flutter and Divergence Boundary Comparison

The converged flutter boundary for each of the cases considered herein can be compared to results for similar configurations from the literature (12) as shown in Figure 16. All cases shown are results for a simply supported plate. The aspect ratio of the plate, $\frac{a}{b}$, varies from the results in the previous literature but is the same for both cases considered herein. The Case 1 SSSS result is directly comparable to the results from the literature having the same simply supported boundary conditions on all sides. Consistent with the trend of increasing $\frac{a}{b}$ ratio, the Case 1 SSSS flutter dynamic pressure result, where $\frac{a}{b} = 1.5$, is higher than both cases from the literature which have $\frac{a}{b}$ ratios of $\frac{a}{b} = 0$ and $\frac{a}{b} = 1.0$ respectively. The flutter dynamic pressure boundary of Case 2 SSSF is higher than that of Case 1 SSSS, a surprising and important result. The major difference between the two cases is the trailing edge boundary condition. Based on these results, the free trailing edge requires a higher dynamic pressure to achieve instability and is therefore more stable than the plate with all edges simply supported.

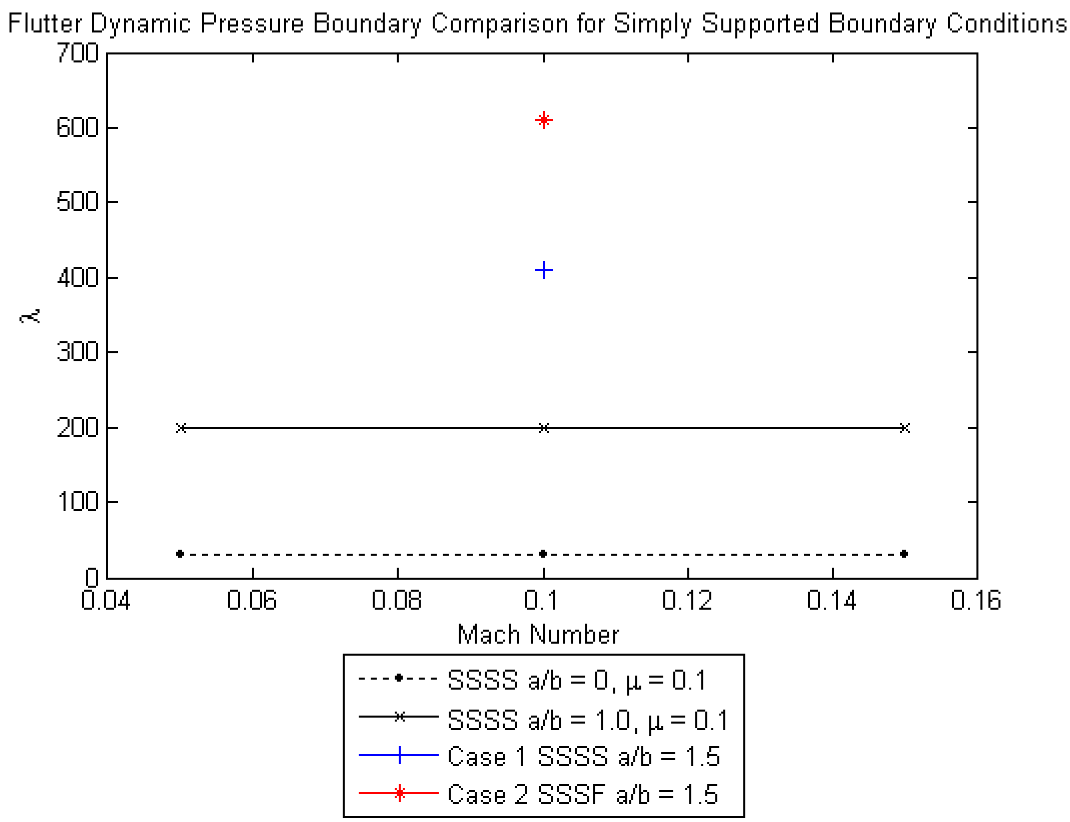

Figure 16 Flutter dynamic pressure boundary comparison for simply supported boundary condition cases

5.2. System 2. Clamped Plate Model

5.2.1. Natural Frequency

The natural frequencies for the two clamped cases presented herein are summarized in Figure 17. As with the simply supported cases, the natural frequencies of Case 3 CCCF, with the free trailing edge, are lower than the case in which all edges are fixed, Case 4 CCCC. Unlike the simply supported cases, there is some coupling between the modes due to beam modes used to describe the model system. The natural frequencies presented are determined from a full 12 mode calculation. It should be noted that the natural frequencies presented are distinct; the lines connecting the values are to facilitate visualization of differences between the cases.

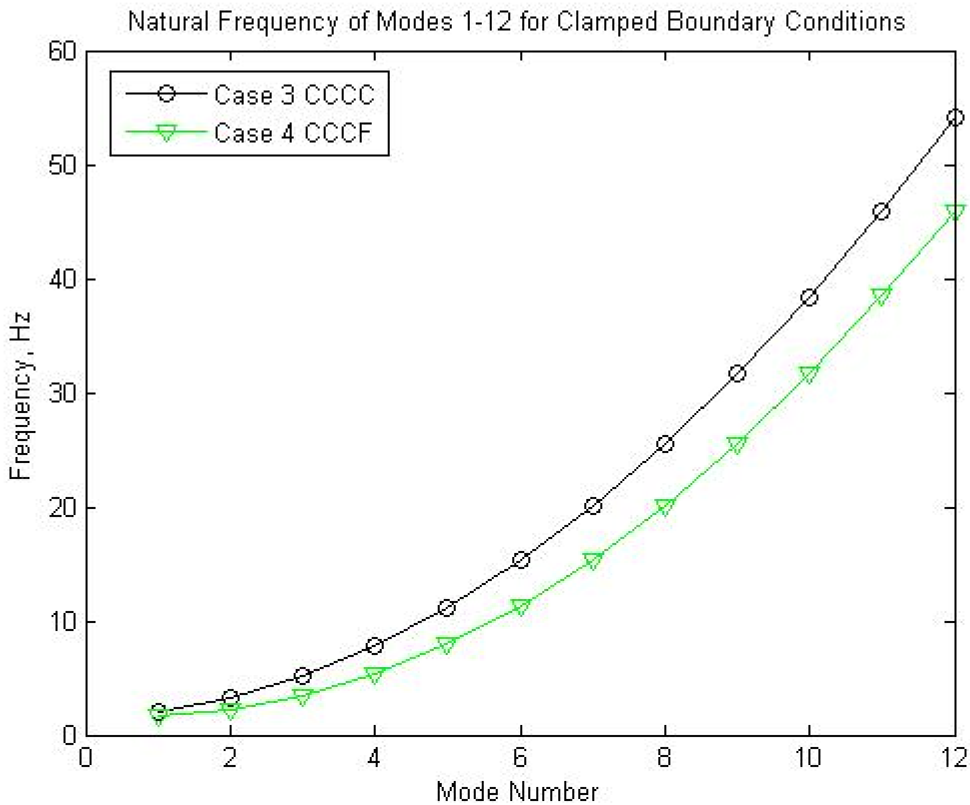

Figure 17 Natural frequency of modes 1-12 for clamped boundary condition cases

5.2.2. Flutter and Divergence Calculations

The convergence of the flutter or divergence dynamic pressure boundary for the clamped cases is presented in Figure 18. Below the flutter boundary, time history calculations result in stable behavior usually manifest as damped oscillations. Above the flutter or divergence boundary, the plate behavior is unstable, resulting in either divergence or flutter.

Case 3 CCCC initially appears to converge with fewer than four modes, however the addition of more than 4 modes leads to a sharp drop and oscillation of the stability boundary before reconvergence with at least nine modes. With more than nine modes however, the flutter boundary does appear completely converged.

Case 4 CCCF conversely, also exhibits a drop in the flutter boundary; however instead of oscillating like the previous case, it appears to move asymptotically toward a converged result with the inclusion of additional modes.

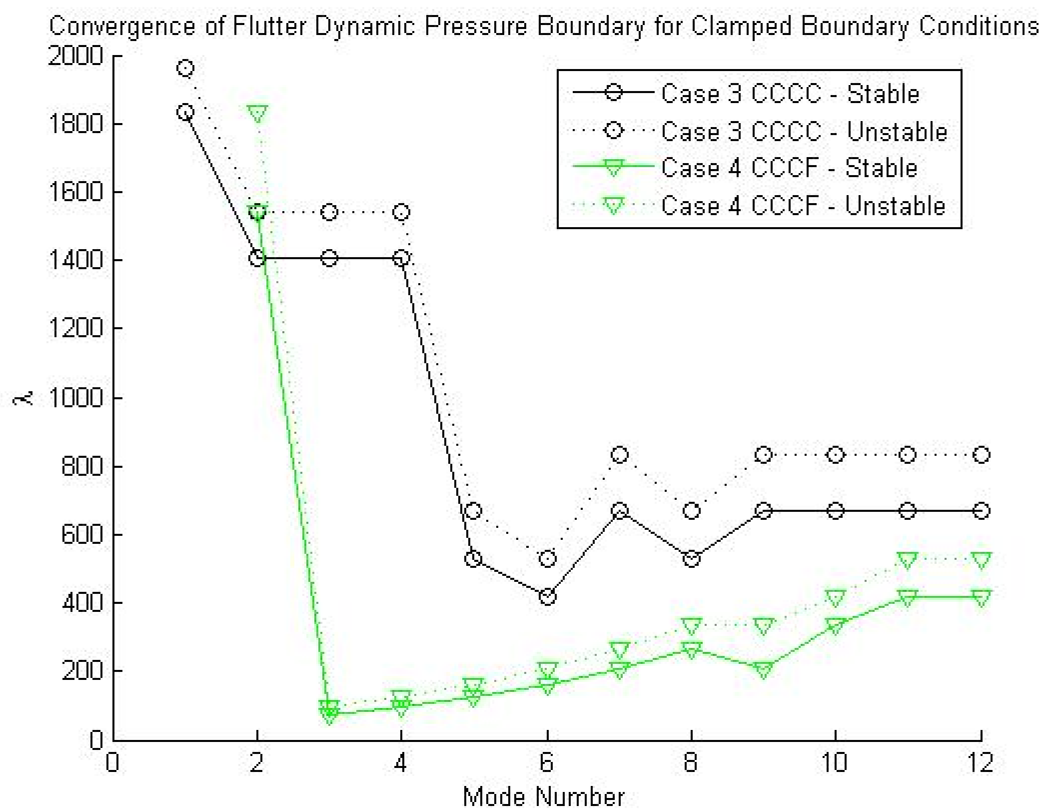

Figure 18 Convergence of flutter dynamic pressure boundary for clamped boundary condition cases

5.2.3. Convergence

For Case 3 CCCC, convergence of the flutter dynamic pressure is confirmed when we observe the frequency content of the time histories just beyond the flutter boundary. Figure 19 allows a comparison of the frequency content of the unstable system with the dynamic pressure set to a value at which the instability is manifest. Stability at a relatively high dynamic pressure is seen when up to four modes are included in the calculation. However the frequency content jumps between a dominating first and sixth mode when between five and eight modes are included in the computation. When more than eight modes are included however, the frequency settles to a value slightly lower than the sixth mode natural frequency. The dynamic pressure has also stabilized at a new lower value indicating convergence. As with the previously discussed Case 2 SSSF, which has a different set of boundary conditions and a free trailing edge, the fifth and sixth modes are combining to dominate the flutter behavior as further indicated by the amplitude of the oscillations observed in the time histories.

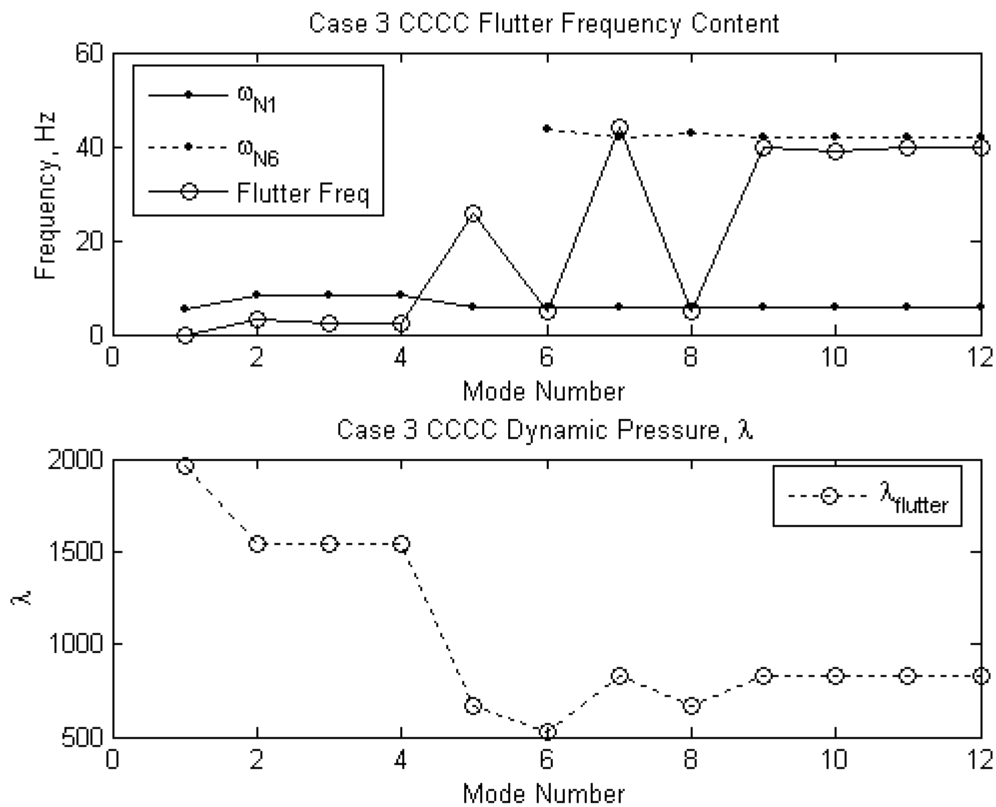

Figure 19 Flutter frequency convergence and dominant mode identification for Case 3 CCCC

The same comparison between the flutter dynamic pressure and frequency content for Case 4 CCCF is shown in Figure 20. In this case, the frequency content of the unstable system is dominated largely by the second mode with some influence from the third. The dynamic pressure appears settled with 12 modes included in the calculations, however the climb of the dynamic pressure, λ, from three modes to twelve modes covers a span of several hundred and as a result is the least converged case of the four presented.

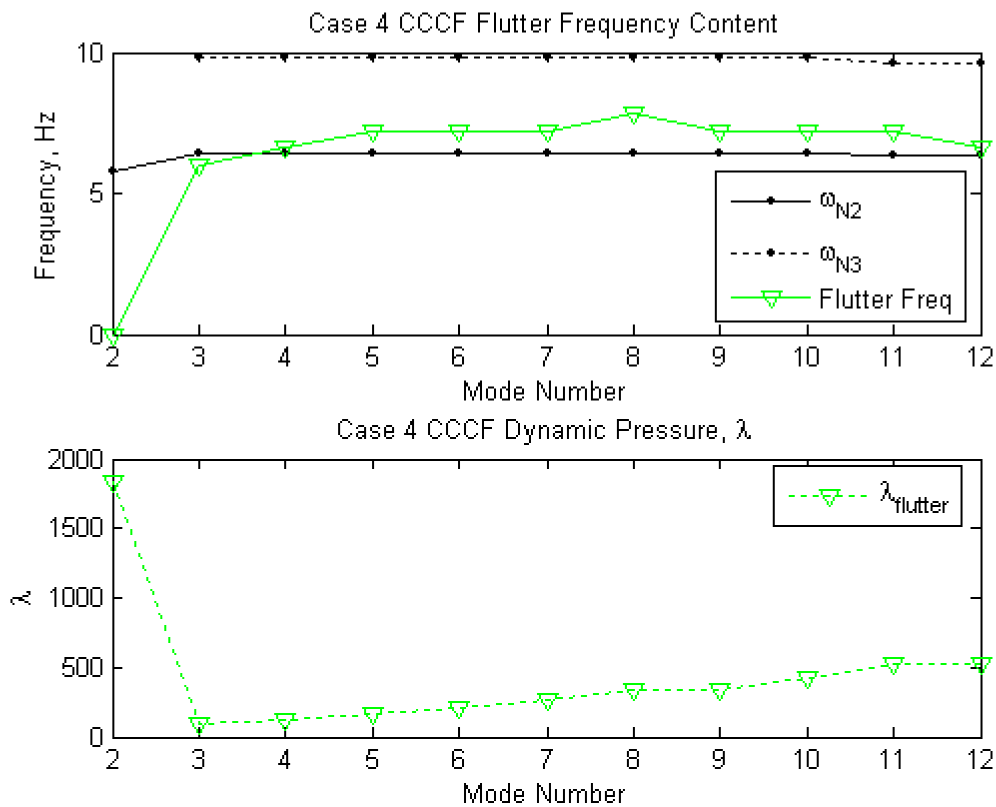

Figure 20 Flutter frequency convergence and dominant mode identification for Case 4 CCCF

5.2.4. Flutter Boundary Comparison

Unlike with the previous cases, the clamped cases do not have comparable literature values to compare. We can however compare the four cases presented herein.

Figure 21 shows the relative flutter boundaries of the four cases considered herein compared to the two cases previously used for comparison purposes from the literature. As can be seen, all four cases are of a similar magnitude and separation within each system.

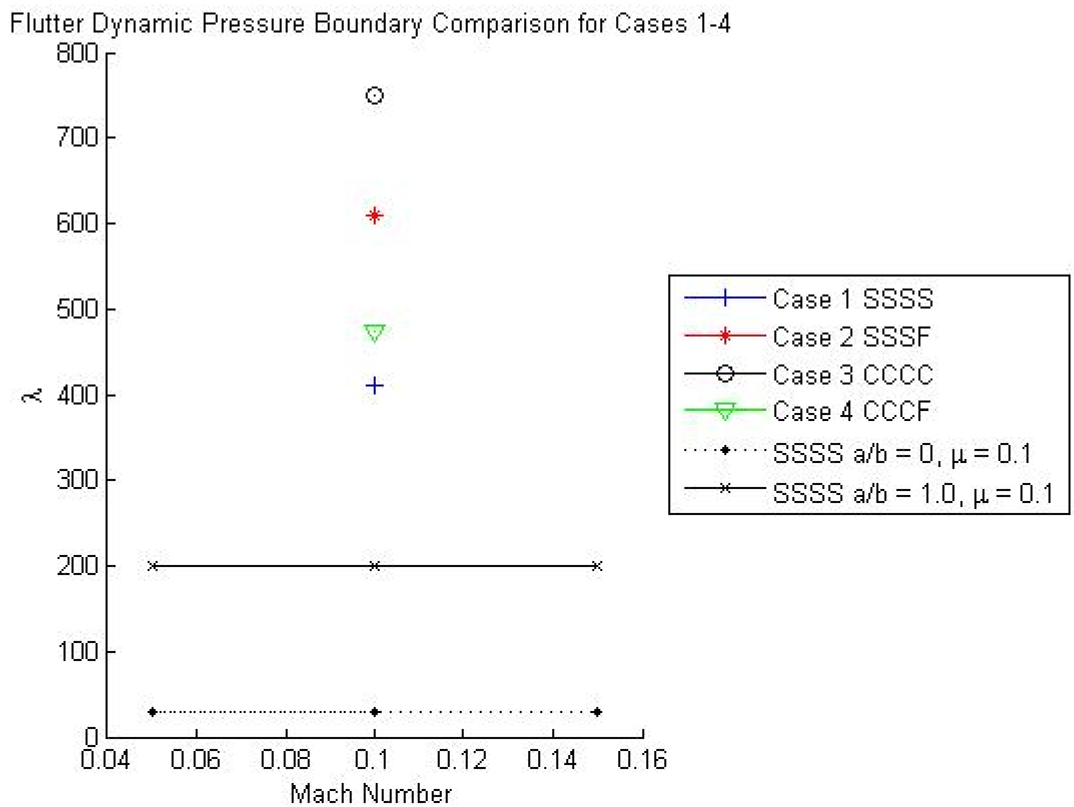

Figure 21 Flutter dynamic pressure boundary comparison for Cases 1-4

Interestingly, the two systems switch behavior trends, for the simply supported cases, the free trailing edge serves to stabilize the system, while with clamped boundary conditions, the free trailing edge lowers the stability and the dynamic pressure at which the system goes unstable. The flutter modes are shown in Figure 22. Each was reconstructed from amplitude data collected from the time history for converged flutter parameter set for each case. In general, the two cases whose flutter behavior are dominated by higher modes, Case 2 SSSF and Case 3 CCCC, have higher stability boundaries and are more stable than the two cases whose instability is dominated by lower modes, Cases 1 SSSS and 4 CCCF. The similarity in the dominant modes is striking in each case.

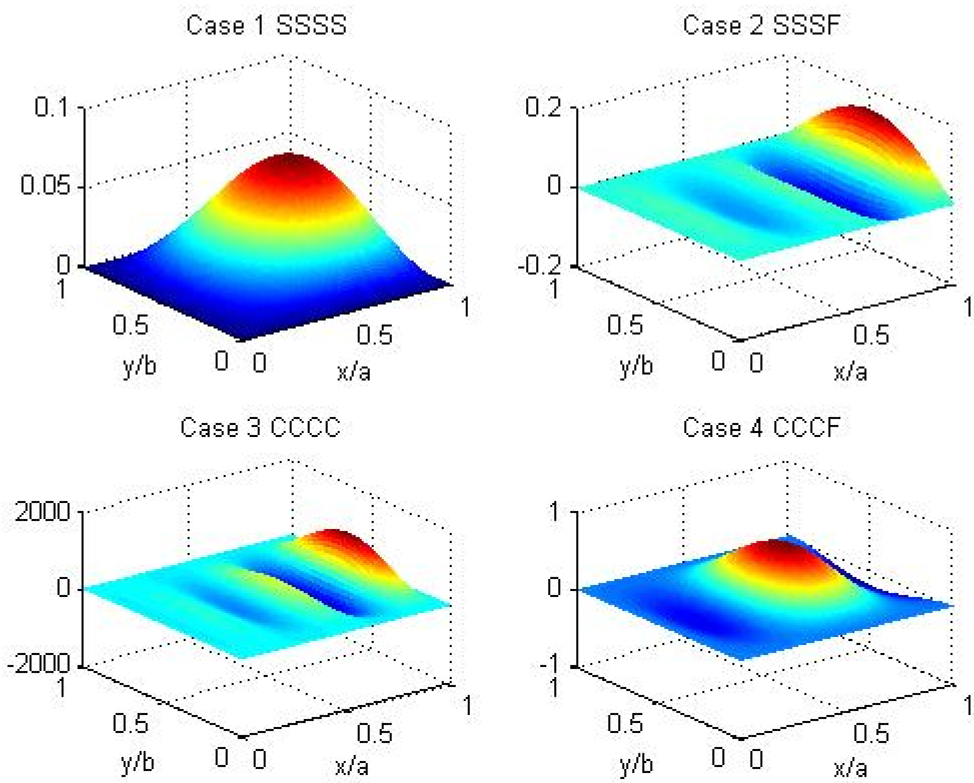

Figure 22 Flutter mode shapes for Cases 1-4

In addition, it should be noted that relative to $\frac{a}{b}$ ratio, the dynamic pressure boundaries for the clamped cases is comparable to that of the simply supported cases with the same aspect ratio.

.

6. Discussion and Conclusions

The results shown in the previous section are a novel contribution to the understanding of fundamental aeroelastic plate dynamics. In addition to increasing the fundamental understanding of the configurations presented, as anticipated, the two systems and the four cases clearly demonstrate a strong variability closely tied to the boundary conditions of the structure. What follows is a summary and discussion of the conclusions reached from analysis of the results and their contribution to the state of the art.

6.1. System 1. Simply Supported Plate Model

Aeroelastic analysis of a plate with simply supported boundary conditions was considered. Two configurations, the first with all edges simply supported and the second with the leading and side edges simply supported and trailing edge free were considered. Both cases considered exhibited higher flutter dynamic pressure boundaries compared to similar configurations but for lower length to width ratios from the literature. Consistent with previous results, the higher $\frac{a}{b}$ ratio of the all edges simply supported case examined herein resulted in a higher flutter dynamic pressure boundary than smaller $\frac{a}{b}$ ratios with the same boundary conditions. The free trailing edge case resulted in a higher flutter dynamic pressure boundary for the same $\frac{a}{b}$ ratio. The flutter boundary for the free trailing edge case was also determined to be dominated by a much higher mode and required a large number of modes to achieve convergence compared to the all edges simply supported cases calculated here and presented in the literature.

6.2. System 2. Clamped Plate Model

Aeroelastic analysis of a plate with clamped boundary conditions was then considered. As in the previous system, two configurations were considered, the first with all edges clamped and the second with the leading and side edges clamped, the trailing edge free. Both cases exhibited higher flutter dynamic pressure boundaries on the same order of magnitude as the cases with simply supported boundary conditions. However, in a departure from the previous system, the clamped boundary cases reversed the stability trend noted in the previous system. In the two cases considered, constraining the trailing edge of the plate led to a higher flutter dynamic pressure than when the trailing edge was free. Releasing the trailing edge resulted in a lower, more unstable flutter boundary. The previously presented cases, with simply supported boundaries, exhibited the opposite behavior. It must also be noted, however that for the two cases with lower flutter dynamic pressure boundaries, Case 1 SSSS and Case 4 CCCF, the instability of the system is dominated by low modes, usually a combination of the first, second and third modes, and at a low modal frequency. In contrast, the cases with a higher stability boundary, Case 2 SSSF and Case 3 CCCC exhibit their instability in much higher modes, in both cases a combination of the fifth and sixth modes at a much higher frequency, and in each case convergence does not occur until a large number of modes is included. The stability of both cases is driven by the first and second modes when fewer modes are included.

Despite this reversal, the flutter boundary was nominally consistent in its magnitude with the $\frac{a}{b}$ ratio trend noted in the discussion of the previous system. This continues to indicate some level of confidence in the result. To further validate the computational results presented herein, a series of experiments are required to verify the accuracy of both the model assumptions and the resulting flutter boundary calculations. This work would also confirm the objective question of which system best captures the behavior of the physical system.

Finally, the frequency content of the flutter behavior in all four cases studied is at the low end of the human hearing range which is commonly reported to be between 20 Hz and 20 kHz. Dominant frequencies were reported to be around 4-5 Hz or around 40 Hz. Allowing for some variability in the result, this suggests that a careful study of the anticipated acoustic reduction versus the introduced acoustic signature will need to be carefully analyzed prior to implementation.

7. Future Work

There are several phases of further work, both theoretical and experimental, that will serve to complement and enhance the results presented herein.

7.1. Theory

On the theoretical front, there are several interesting avenues down which to travel. As previously indicated, additional analysis of the effect that Mach number has on the flutter boundary trend would serve to validate the method against results presented in the literature (12). This analysis would require the additional computation of influence functions for each mode at these new Mach numbers and would therefore be resource intensive in execution.

An additional avenue of exploration might also include the additional configuration of freeing the leading edge. Work in this direction has been initiated, but not included here. This configuration is likely of particular interest as it alleviates the design constraint of the leading edge being constrained and is not well addressed in the literature.

Additional verification of the method might also be performed using an alternative method, and in conjunction with colleagues, this avenue is also being explored.

Following verification of the linear model, additional analysis can be undertaken to analyze the more complicated flow field and structural parameters likely to exist in actual deployment. Some work by NASA engineers has been undertaken to address these questions and inform experimental design and testing.

7.2. Experiment

Experimental results are of particular interest to the validation of the results presented herein. The first phase of experimental results would analyze the structural properties of the material in the considered configurations to determine if the models adequately capture physical behaviors like natural frequency. Additional experimentation would then utilize a wind-tunnel to model the coupled aeroelastic system and observe the flutter or divergence boundary while measuring the dominant modal content both in shape and frequency as well as modal amplitude to determine if non-linear effects dominate .

Following verification of the linear model and its behavior, additional experimentation, like that planned to take place at NASA LaRC, would verify the behavior of a more realistically designed test article to determine if the linear model accurately informs the behavior of the more complex system.

Bibliography

1. NASA. *National Aeronautics and Space Administration: Strategic Plan 2000.* Washington, DC : NASA Headquarters, 2000.

2. FAA. FAA Long-Range Aerospace Forecasts. *Federal Aviation Administration.* [Online] [Cited: December 9, 2010.] http://www.faa.gov/data_research/aviation/long-range_forecasts/.

3. NASA. Noise. *www.nasa.gov.* [Online] 2009. [Cited: December 9, 2010.] NF-2009-03-489-HQ.

4. Swenson, Harry, Barhydt, Richard and Landis, Michael. *Next Generation Air Transportation System (NGATS) Air Traffic Management (ATM)-Airspace Project: Reference Material, External Release Version.* s.l. : NASA, 2006.

5. NASA. NASA Fundamental Aeronautics: The Subsonic Fixed Wing Project. [Online] September 9, 2009. [Cited: December 8, 2010.] http://www.aeronautics.nasa.gov/fap/sfw_project.html.

6. Collier, Fay, Zavala, Eddie and Huff, Dennis. *Fundamental Aeronautics Program: Subsonic Fixed Wing Project Reference Document.* s.l. : NASA, 2006.

7. *Multi-Objective Leading Edge Concepts for Airframe Noise Reduction.* Turner, T.M. Atlanta, GA : NASA Fundamental Aeronautics Program, Third Annual Technical Conference on Disc [CD-ROM], 2009.

8. Choudhari, Meelan M., et al. *Aeroacoustic Experiments in the Langley Low-Turbulence Pressure Tunnel.* Hampton, Virginia : National Aeronautics and Space Administration, 2002. NASA/TM-2002-211432.

9. *In Search of the Physics: The Interplay of Experimental and Computation in Airframe Noise Research; Flap-Edge Noise.* Streett, C.L., et al. NASA Langley Research Center, Hampton, VA, USA : AIAA 41st Aerospace Sciences Meeting and Exhibit, Reno, NV, January 6-9, 2003.

10. *Aerodynamic Noise Reduction for High-Lift Devices on a Swept Wing Model.* Streett, C.L., et al. Reno, NV : 44th AIAA Aerospace Sciences Meeting and Exhibit, 2006. AIAA 2006-212.

11. *An Analytical Assessment of NASA's N+1 Subsonic Fixed Wing Project Noise Goal.* Berton, Jeffrey J., Envia, Edmane and Burley, Casey L. Miami, FL : 15th AIAA/CEAS Aeroacousitcs Conference, 2009. Vols. 11-13 May.

12. Dowell, E.H. *Aeroelasticity of Plates and Shells.* Leyden : Noordhoff International Publishing, 1975.

13. *Flutter and Limit cycle oscillations of two-dimensional panels in three-dimensional axial flow.* Tang, D.M., Yamamoto, H. and Dowell, E.H. s.l. : Journal of Fluids and Structures, 2003, Vol. No. 17.

14. *Power extraction from aeroelastic limit cycle.* Dunnmon, J.A., Stanton, S.C., Mann, B.P., Dowell, E.H. s.l. : Journal of Fluids and Structures, March 2011, Vol. Available online 16 March 2011.

15. Stanton, Samuel C. *Energy Harvesting from Turbulent Boundary Layer Pressure Fluctuations with Aeroacoustic Coupling: A Stochastic Optimal Control Approach [M.S. Thesis].* Durham, NC : Duke University, 2008.

16. *On Aymptotic Approximations to Beam Model Shapes.* Dowell, E. H. s.l. : Journal of Applied Mechanics, 1984, Vol. 51.

17. Bisplinghoff, Raymond L., Ashley, Holt and Halfman, Robert L. *Aeroelasticity.* Mineola, New York : Dover Publications, Inc., 1955, 1983. ISBN 0-486-69189-6.

18. *Generalized Aerodynamic Forces on a Flexible Plate Undergoing Transient Motion.* Dowell, Earl H. 4, s.l. : Quarterly of Applied Mathematics, 1966, Vol. XXIV.

19. Poisson's Ratio. *Wikipedia.* [Online] Wikimedia, February 27, 2011. [Cited: 3 15, 2010.] http://en.wikipedia.org/wiki/Poisson%27s_ratio.

20. Shapiro, Ascher H. *The Dynamics and Thermodynamics of Compressible Fluid Flow.* New York : The Ronald Press Company, 1953. 53-8869.